

The origin of very-high-energy gamma-rays from GRB 221009A: implications for reverse shock proton synchrotron emission

B. Theodore Zhang^a, Kohta Murase^{b,c,d,a}, Kunihiro Ioka^a, Bing Zhang^{e,f}

^aCenter for Gravitational Physics and Quantum Information, Yukawa Institute for Theoretical Physics, Kyoto University, , Kyoto, Kyoto 606-8502, , Japan

^bDepartment of Physics, The Pennsylvania State University, , University Park, PA 16802, , USA

^cDepartment of Astronomy & Astrophysics, The Pennsylvania State University, , University Park, PA 16802, , USA

^dCenter for Multimessenger Astrophysics, Institute for Gravitation and the Cosmos, The Pennsylvania State University, , University Park, PA 16802, , USA

^eNevada Center for Astrophysics, University of Nevada, , Las Vegas, NV 89154, , USA

^fDepartment of Physics and Astronomy, University of Nevada Las Vegas, , Las Vegas, NV 89154, , USA

Abstract

Recently, GRB 221009A, known as the brightest of all time (BOAT) GRB, has been observed across an astounding range of ~ 18 orders of magnitude in energy, spanning from radio to very-high-energy (VHE) bands. Notably, the Large High Altitude Air Shower Observatory (LHAASO) recorded over 60000 photons with energies exceeding 0.2 TeV, including the first-ever detection of photons above 10 TeV. However, explaining the observed energy flux evolution in the VHE band alongside late-time multi-wavelength data poses a significant challenge. Our approach involves a two-component structured jet model, consisting of a narrow core dominated by magnetic energy and a wide jet component dominated by matter. We show that the combination of the forward shock electron synchrotron self-Compton emission from the two-component structured jet and reverse shock proton synchrotron emission from the wide jet could account for both the energy flux and spectral evolution in the VHE band, and the early TeV lightcurve may be influenced by prompt photons which could explain the initial steep rising phase. We notice the arrival time of the highest energy photon ~ 13 TeV detected by LHAASO, especially a minor flare and spectral hardening occurring about ~ 500 - 800 seconds after the trigger, is consistent with the emergence of the reverse shock proton synchrotron emission. These findings imply that the GRB reverse shock may serve as a potential accelerator of ultra-high-energy cosmic rays, a hypothesis that could be tested through future multimessenger observations.

Keywords: gamma-ray burst: general, gamma-rays: stars, radiation mechanisms: non-thermal

1. Introduction

The detection of very-high-energy (VHE) gamma rays (with energies ranging from 0.1 TeV to 100 TeV) originating from gamma ray bursts (GRBs) marks a significant advancement in our ability to explore the physics of GRBs and their associated radiative processes (See Mészáros, 2006; Kumar and Zhang, 2014; Zhang, 2018, for a review). The initial detections in the VHE band included GRB 190114C observed by the Major Atmospheric Gamma Imaging Cherenkov (MAGIC) telescopes (Acciari et al., 2019b,a) and GRB 180720B observed by the High Energy Stereoscopic System (H.E.S.S.) (Abdalla et al., 2019). Subsequently, VHE gamma rays from GRB 190829A (Abdalla et al., 2021) and GRB 201216C (Blanch et al., 2020b) were also reported. Furthermore, there are two sub-threshold events, namely GRB 160821B (Acciari et al., 2021) and GRB 201015A (Blanch et al., 2020a). The four significantly detected VHE GRBs are long GRBs (Noda and Parsons, 2022), and all these detections align with the hypothesis that VHE gamma rays originate during the afterglow phase when the relativistic outflow enters the self-similar deceleration

phase (Zhang, 2019; Miceli and Nava, 2022). However, it is worth noting that both MAGIC and H.E.S.S. operate as Imaging Atmospheric Cherenkov Telescopes (IACTs), characterized by limited fields of view and the necessity for longer slew times to perform follow-up observations. Consequently, the detection of VHE gamma rays from the early afterglow, especially during the prompt phase, presents a formidable challenge.

On October 9, 2022, the Fermi gamma ray Burst Monitor (Fermi-GBM) detected GRB 221009A at $T_0 = 13:16:59.99$ UT (Lesage et al., 2023). Because of the highest fluence during the prompt phase, GRB 221009A has been referred to as the brightest of all time (BOAT) (Burns et al., 2023). Furthermore, this GRB was also captured by the Large High Altitude Air Shower Observatory (LHAASO), an extensive air shower detector designed for gamma ray observations (Ma et al., 2022). A detailed analysis of LHAASO's Water Cherenkov Detector Array (WCDA) data unveiled more than 64000 photons with energies ranging from 0.2 TeV to 7 TeV that can be attributed to GRB 221009A within the first $T - T_0 \sim 3000$ seconds following the Fermi-GBM trigger at T_0 (Cao et al., 2023a). Moreover, the LHAASO-KM2A detector also registered dozens of photons with energies exceeding ~ 7 TeV, with the highest recorded photon energy surpassing 10 TeV (Cao et al., 2023b). Notably,

Email addresses: bing.zhang@yukawa.kyoto-u.ac.jp (B. Theodore Zhang), murase@psu.edu (Kohta Murase)

the observed flux ratio between TeV and MeV emission during the main burst phase is $\lesssim 2 \times 10^{-5}$, possibly due to internal $\gamma\gamma$ absorption (Cao et al., 2023a). For the first time, we observed the rising phase of energy flux in the VHE band, which reached its peak flux at $T_0 + 244$ s and then gradually declined over time. This smooth temporal profile of the TeV light curve aligns with its origin in the afterglow phase (Cao et al., 2023a).

Multiple studies lend support to the idea that VHE gamma rays originate during the afterglow phase. In this scenario, the standard synchrotron self-Compton (SSC) process plays a pivotal role in generating the observed VHE gamma rays (Meszaros and Rees, 1994; Dermer et al., 2000; Sari and Esin, 2001; Zhang and Meszaros, 2001). In the SSC model, the same group of electrons responsible for synchrotron emission can upscatter these photons to higher energies by a factor of approximately γ_e^2 , where γ_e represents the electron Lorentz factor. This SSC framework is consistent with the emissions observed in many VHE GRBs (e.g., Acciari et al., 2019b; Abdalla et al., 2019; Wang et al., 2019; Asano et al., 2020; Derishev and Piran, 2021; Zhang et al., 2021; Huang, 2022), although the simplistic one-zone model appears challenging for some VHE GRBs, such as GRB 190829A (e.g., Abdalla et al., 2021; Salafia et al., 2022; Sato et al., 2023b; Ren et al., 2023; Khangulyan et al., 2023; Sato et al., 2023a). Nevertheless, it remains unclear whether the SSC process is the sole mechanism responsible for producing VHE gamma rays in GRBs. An alternative process that warrants consideration is the external inverse-Compton (EIC) mechanism, particularly in scenarios where the prompt emission coincides with the early afterglow phase (Wang et al., 2006; Murase et al., 2010; Toma et al., 2009; Murase et al., 2011; He et al., 2012; Veres and Mészáros, 2014; Murase et al., 2018). Recent studies lend credence to the EIC scenario as a viable alternative for VHE gamma ray production, especially when considering the presence of a long-lasting central engine (Zhang et al., 2021b) and/or flares (Zhang et al., 2021a).

VHE gamma ray production may also involve hadronic processes associated with the acceleration of cosmic ray protons and ions. In the realm of high-energy astrophysical sources featuring relativistic jets, extensive research has focused on proton synchrotron emission (e.g., Totani, 1998b; Zhang and Meszaros, 2001; Murase et al., 2008; Asano et al., 2009) and photomeson production processes (e.g., Waxman and Bahcall, 2000). However, the absence of high-energy neutrinos from GRBs imposes stringent constraints on the efficiency of the photomeson production process (e.g., Murase et al., 2022; Ai and Gao, 2023; Liu et al., 2023; Rudolph et al., 2023; Abbasi et al., 2023). Conversely, the radiative efficiency of the proton synchrotron process is considerably lower than that of electrons, necessitating the acceleration of protons to ultra-high-energies (UHE, exceeding 1 EeV). Isravel et al. (2023b) utilized synchrotron emission from UHE protons, accelerated within the external forward shock, to account for the observed VHE gamma rays in GRB 190114C, with the SSC component in a subordinate role. Similarly, Huang et al. (2023a) examined UHE protons accelerated during the prompt emission phase and injected into the afterglow jet, demonstrating that proton syn-

chrotron emission could dominate the early TeV afterglow of GRB 190829A. Inspired by the detection of $\gtrsim 10$ TeV photons from GRB 221009A, Zhang et al. (2023) put forward the idea that reverse shock proton synchrotron emission could be a significant contributor to VHE gamma ray production in the case of GRB 221009A (See Isravel et al., 2023a, for the external forward shock model.).

Studying the production of VHE gamma rays in detail is crucial, especially considering the remarkable TeV flux light curve observed by LHAASO and the wealth of multiwavelength data available. In their study Cao et al. (2023a), they conducted comprehensive numerical modeling of the TeV light curve, focusing on the time window covered by LHAASO's observations. They found that the early TeV emission can be adequately modeled by SSC emission from a narrow jet. On the other hand, the late-time radio to GeV data has to be attributed to a second jet (Sato et al., 2023a; Zheng et al., 2023; Zhang et al., 2023). While the TeV light curve suggests a preference for a constant external medium density distribution¹ (Cao et al., 2023a; Sato et al., 2023a), the late-time radio afterglow aligns with the propagation in a wind medium (Ren et al., 2023; Gill and Granot, 2023). In our earlier work of Zhang et al. (2023), we focused on the moment when the reverse shock has fully traversed the ejecta, marking the point at which the reverse shock emission attains its peak luminosity. Interestingly, our analysis revealed that proton synchrotron emission exhibits hard spectra, and the maximum energy of these emissions can surpass 10 TeV. However, Zhang et al. (2023) came out before the availability of the LHAASO data and without considering the realistic dynamical evolution of the jet, so it is reasonable to perform detailed calculations of the reverse shock proton synchrotron model in this work.

In this study, we conduct comprehensive numerical modeling of VHE gamma ray production and multiwavelength light curves using the standard reverse-forward external shock model with a structured jet. We investigate various radiative processes involving nonthermal electrons and protons from both the shocked ejecta and the shocked external medium. Our paper is organized as follows: In Section 2, we provide detailed information about the numerical modeling of the reverse-forward shock emission within the structured jet. In Section 3, we present our findings and compare them to the observed multi-wavelength light curves and energy spectra from GRB 221009A. In Section 4, we discuss the implications of our results. Finally, we summarize our study in Section 5.

In this study, we employ centimetre-gram-second system units and express quantities as $Q = Q_x 10^x$. We denote photon energy in the observer frame as E and in the comoving frame as ε .

2. Physical model

2.1. Structured jet

Structured jets in the context of GRBs have been extensively studied in previous research (Mészáros et al., 1998; Rossi

¹Note the wind medium case can not be excluded (Khangulyan et al., 2023).

et al., 2002; Zhang and Meszaros, 2002; Kumar and Granot, 2003; Zhang et al., 2004). The detection of the gravitational wave event GW 170817 (Abbott et al., 2017a) and the associated short GRB 170817A (Abbott et al., 2017b) provides a unique opportunity to explore the characteristics of relativistic jets. The gradually rising radio to X-ray afterglow observations support the off-axis structured jet model (Lazzati et al., 2018; Margutti et al., 2018; Troja et al., 2018; Ioka and Nakamura, 2018). Structured jet formation is a natural outcome when the jet interacts with the stellar envelope (Gottlieb et al., 2020a,b). Interestingly, the fitting of the TeV light curve suggests a preference for emission from a narrow jet, which may correspond to the core of a structured jet (Cao et al., 2023a). Furthermore, the observed X-ray decay rate is shallower than the predicted post-jet-break index for a standard top-hat jet, suggesting that relativistic jets likely exhibit angular structure in their energy profiles (O'Connor et al., 2023; Gill and Granot, 2023).

In this study, we present an illustrative representation of a structured jet, which consists of a magnetic-dominated narrow core and a matter-dominated wide jet component, as depicted in Fig. 1. The arguments in support of such a two-component jet with different jet compositions have been presented in detail in Zhang et al. (2023). The magnetic-dominated narrow core is represented as a top-hat jet with a uniform energy and velocity distribution. Conversely, the matter-dominated wide jet component is modeled as a power-law structured jet.

We define $\mathcal{E}(\theta)$ as the angle-dependent isotropic-equivalent energy of a given structured jet. For the power-law structured jet, we have (e.g. Takahashi et al., 2022)

$$\mathcal{E}(\theta) = \mathcal{E}_k \left[1 + \left(\frac{\theta}{\theta_c} \right)^2 \right]^{-a/2} \quad (\theta < \theta_j), \quad (1)$$

where \mathcal{E}_k represents the isotropic-equivalent kinetic energy, θ_c is the narrow cone angle, a is the power-law index, and θ_j is the jet half-opening angle. The distribution of the Lorentz factor is described as

$$\Gamma(\theta) = \Gamma_0 \left[1 + \left(\frac{\theta}{\theta_c} \right)^2 \right]^{-a/2} \quad (\theta < \theta_j), \quad (2)$$

where Γ_0 is the initial bulk Lorentz factor of the ejecta. In the case of a uniform top-hat jet, $a = 0$.

2.2. Ambient medium

Late-time modeling of the radio afterglow from GRB 221009A suggests that the external medium follows a wind profile, which decreases outwards as $n_{\text{ex}}(R) \propto R^{-2}$ (e.g., Ren et al., 2023; Gill and Granot, 2022). However, the slow rise in VHE band energy flux, characterized by a slope of approximately 1.8, suggests a preference for either a constant ambient density distribution near the progenitor or energy injection in the wind medium (Cao et al., 2023a). The transition from a constant ambient density to a wind medium leads to a change in the slope of the multiwavelength light curve. It's important to note that the early afterglow light curve may be shaped by $\gamma\gamma$

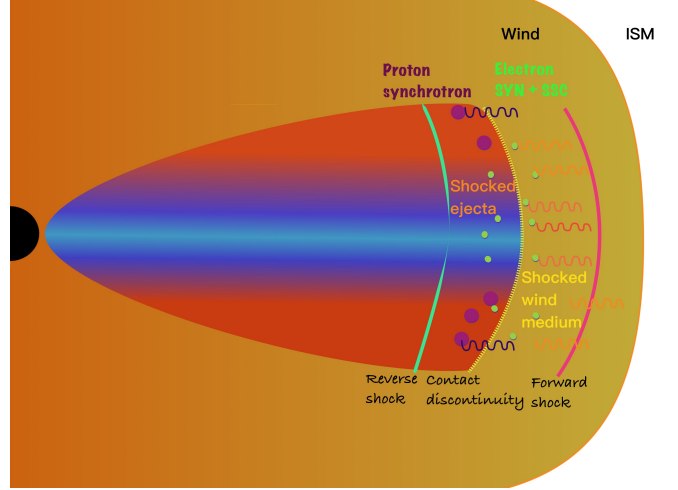


Figure 1: A schematic depiction of the structured jet, featuring a magnetic-energy-dominated narrow core (illustrated with blue color) and a matter-dominated wide jet component (illustrated with red color).

attenuation from external prompt photons (e.g., Zhang et al., 2023; Khangulyan et al., 2023).

In our study, we consider a scenario where the external medium is predominately composed of a stellar wind. However, in the inner region near the progenitor star, the density profile of the external medium could be influenced by pre-explosion burst activities, resulting in a constant density profile. We model the external medium using the following formula,

$$n_{\text{ex}}(R) = \min[n_{\text{ex},0}, AR^{-k}], \quad (3)$$

where $A = 3 \times 10^{35} A_* \text{cm}^{-1}$ and $k = 2$ for a stellar wind medium. The parameter A_* represents the ratio of mass-loss rate to wind speed, normalized to $10^{-5} M_\odot \text{yr}^{-1} / 10^3 \text{km s}^{-1}$. The number density distribution of the external medium is illustrated in Fig. 2.

2.3. Particle acceleration and radiative process

As the relativistic ejecta interacts with the external medium, two shocks form: the forward shock, advancing into the ambient external medium, and the reverse shock, moving backward to decelerate the outflow. In this context, we denote the downstream internal energy density (pressure) of the shocked wind medium as e_2 (p_2) and the downstream internal energy density (pressure) of the shocked ejecta as e_3 (p_3), as depicted in Fig. 1. Given pressure equilibrium across the contact discontinuity, described by $p_2 = p_3$, we find the relation

$$(\hat{\gamma}_2 - 1)e_2 = (\hat{\gamma}_3 - 1)e_3, \quad (4)$$

where $\hat{\gamma}_2$ and $\hat{\gamma}_3$ represent the adiabatic indices in shocked ejecta and shocked external medium, respectively. The adiabatic indices can be expressed as

$$\hat{\gamma} \approx \frac{4\bar{\gamma} + 1}{3\bar{\gamma}}, \quad (5)$$

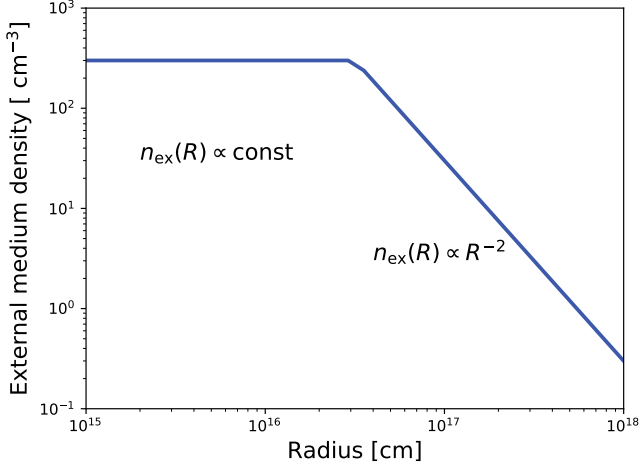


Figure 2: The number density distribution of the external medium as a function of radius from the central engine in the laboratory frame. Here, we adopt $n_{\text{ex},0} = 300 \text{ cm}^{-3}$ and $A_* = 1$.

where $\bar{\gamma}$ represents the average Lorentz factor of particles. For non-relativistic case, $\bar{\gamma} = 5/3$, whereas for relativistic case, $\bar{\gamma} = 4/3$ (Zhang, 2018).

The amplification of magnetic field strength in the downstream region of the reverse-forward shock system remains unclear (e.g., Medvedev and Loeb, 1999). We parameterize a fraction ϵ_B (ϵ'_B) of the downstream internal energy density of the shocked external matter (ejecta) being converted into magnetic field energy density, u_B (u'_B). Note we use the superscript r to represent the parameters in the shocked ejecta. Both electrons and protons (or ions) can be accelerated as they traverse the shock under the diffusive shock acceleration mechanism (DSA) (e.g., Sironi et al., 2015). These accelerated particles exhibit a power-law distribution, with their maximum energy determined by the balance between the acceleration timescale and various energy loss timescales (e.g., Asano et al., 2020). The electron and proton spectral index are denoted as s'_e and s'_p , respectively. However, the energy content of these nonthermal particles remains unknown. We assume a fraction ϵ_e (ϵ'_e) of the downstream internal energy density goes into nonthermal electrons u_e (u'_e), and another fraction ϵ_p (ϵ'_p) of the downstream internal energy density is allocated to nonthermal protons u_p (u'_p). In addition, we assume a number fraction f_e (f'_e) of electrons can be accelerated. These microphysical parameters can potentially be constrained by fitting multi-wavelength afterglow light curves.

Studies have shown that accelerating protons to ultra-high energies (UHE) is a slow process for ultra-relativistic external forward shocks due to the relatively weak magnetic field in the surrounding medium (e.g., Gallant and Achterberg, 1999; Murase et al., 2008; Sironi et al., 2015). Conversely, the reverse shock has been proposed as an alternative acceleration site for accelerating UHECRs (e.g., Waxman and Bahcall, 2000; Murase, 2007; Murase et al., 2008; Zhang et al., 2018). Note we only consider reverse shock emission from the matter-

dominated wide jet, because the reverse shock is suppressed in the magnetic-dominated narrow core Zhang and Kobayashi (2005). Unlike the forward shock, the reverse shock could be either nonrelativistic or only mildly relativistic as shown in Eq. 27 (Sari and Piran, 1995; Sari, 1997). Building upon the concept proposed in Ref. Zhang et al. (2023), we explore the acceleration of UHE protons by the reverse shock and investigate proton synchrotron emission while considering the dynamical evolution of the reverse shock. Ref. Zhang et al. (2023) also considered reverse shock EIC radiation. This component is relevant for explaining the 0.1-10 GeV gamma rays measured by *Fermi*-LAT, which is not the focus of this work. However, one should keep in mind that proton synchrotron emission studied in this work works self-consistently with the EIC model presented in Ref. Zhang et al. (2023).

2.4. Numerical methods

The calculations in this work are based on the Astrophysical Multimessenger Emission Simulator (AMES) code that includes a module to numerically model multi-wavelength emission from GRB afterglows². We expand the GRB-afterglow module to treat emissions from not only an external forward shock but also a reverse shock. For a comprehensive understanding of the dynamic evolution of the reverse-forward shock system and the associated radiative processes, see Appendix Appendix A. Below, we describe the general calculation processes.

The observed flux at a given observation time T could be determined by integrating over the equal-arrival-time-surface (EATS) (e.g., Zhang, 2018). In our calculations, we adopt the thin-shell limit (van Eerten et al., 2010; Ryan et al., 2020; Takahashi and Ioka, 2020; Takahashi et al., 2022). The observed flux can be estimated as follows (e.g. Takahashi et al., 2022)

$$F_E(T) = \frac{1+z}{d_L^2} \int_0^{\theta_j} d\theta \sin\theta \int_0^{2\pi} d\phi \frac{R^2 |\mu - \beta_{\text{sh}}|}{1 - \mu\beta_{\text{sh}}} \times \frac{j_{E_z}}{\alpha_{E_z}} (1 - e^{-\tau_{E_z}})|_{\hat{t}=T_z+\mu R/c}. \quad (6)$$

Here, $F_E = dF/dE$ is the specific flux, T represents the observation time, z is the redshift, $T_z = T/(1+z)$, d_L stands for the luminosity distance of the source, θ denotes the polar angle measured from the jet axis, ϕ represents the azimuth angle, j_{E_z} refers to the emissivity measured in the laboratory frame, α_{E_z} to the absorption factor measured in the laboratory frame, τ_{E_z} to the corresponding optical depth measured in the laboratory frame, and \hat{t} represents the laboratory time. The term μ is given by

$$\mu = \sin\theta \sin\theta_v \cos\phi + \cos\theta \cos\theta_v, \quad (7)$$

which determines the cosine of the angle formed by the radial vector in the (θ, ϕ) direction and the line-of-sight direction on the x-z plane. Here, θ_v corresponds to the viewing angle measured from the jet axis. The shock front velocity divided by the

²<https://github.com/pegasuskmurase/AMES-GRBafterglow>

speed of light is denoted as $\beta_{\text{sh}} = \sqrt{1 - \Gamma_{\text{sh}}^{-2}}$, where $\Gamma_{\text{sh}} = \sqrt{2}\Gamma$. Here, Γ represents the Lorentz factor of the blastwave fluid immediately behind the shock front. In our calculations, we set $T = 0$ as the arrival time when a photon is emitted at the origin at the laboratory time $\hat{t} = 0$. The width of the shocked shell in the laboratory frame is given by

$$w = \frac{R}{4(3-k)\Gamma^2}. \quad (8)$$

The emissivity measured in the laboratory frame is

$$j_{E_z} = \delta^2 j_\varepsilon = \frac{j_\varepsilon}{\Gamma^2(1 - \beta\mu)^2}, \quad (9)$$

where j_ε is the comoving frame emissivity per unit volume per second per solid angle, δ is the Doppler factor, and

$$E_z = E(1+z) = \delta\varepsilon = \frac{\varepsilon}{\Gamma(1 - \beta\mu)}, \quad (10)$$

is the photon energy in the laboratory frame. The absorption coefficient in the laboratory frame is given by

$$\alpha_{E_z} = \Gamma(1 - \beta\mu)\alpha_\varepsilon, \quad (11)$$

where α_ε is measured absorption coefficient in the comoving frame. The corresponding optical depth can be derived via integration over the line of sight,

$$\tau_{E_z} = \int \alpha_{E_z} ds \approx \alpha_{E_z} \Delta s. \quad (12)$$

where Δs represents a finite segment along a ray traveling the shocked region where emitted photons reach the observer at time T . The value of Δs can be expressed as

$$\Delta s = \frac{R}{4(3-k)\Gamma^2|\mu - \beta_{\text{sh}}|}, \quad (13)$$

as shown in Takahashi et al. (2022). In the optically thin limit, Eq. 6 can be simplified as

$$F_E(T) = \frac{1+z}{d_L^2} \int_0^{\theta_j} d\theta \sin\theta \int_0^{2\pi} d\phi R^2 \Delta R j_{E_z}|_{t=T_z+\mu R/c}, \quad (14)$$

where

$$\Delta R = \frac{R}{4(3-k)\Gamma^2(1 - \mu\beta_{\text{sh}})} \quad (15)$$

represents the radial integration path that contributes to the observed flux at a given observation time T .

In this work, we primarily focus on two key attenuation processes: synchrotron self-absorption (SSA), crucial for understanding low-frequency radio emission, and $\gamma\gamma$ pair production, which affects the escape of VHE gamma rays. In the latter situation, the primary targets for interaction are the nearby low-energy synchrotron photons emitted by nonthermal electrons. The absorption coefficient is estimated as

$$\alpha_\varepsilon \approx \frac{1}{ct_{\gamma\gamma}}, \quad (16)$$

where $t_{\gamma\gamma}$ is the comoving frame interaction timescale. Note that we only consider $\gamma\gamma$ attenuation by the target photons produced in the same shell. It is possible that interactions with target photons from other shells could also contribute to attenuation. However, the density of the target photons from these other shells would be diluted due to expansion after crossing the emitting shell. During our numerical calculation process, we initially overlook the $\gamma\gamma$ attenuation caused by prompt photons. However, we later account for this effect in a subsequent post-processing step, which we detail in the next section. Note in our calculations, we perform calculations in the momentum space, where the *Deep Newtonian* limit is avoided (Huang and Cheng, 2003; Sironi and Giannios, 2013; Wei et al., 2023; Ryan et al., 2023).

3. VHE gamma rays from GRB afterglow

3.1. Early afterglow in the VHE band

Our result is shown in Fig. 3, calculated using the updated GRB module of the AMES code described above. In the upper panel of Fig. 3, we compare numerical results with energy flux measurements by LHAASO-WCDA integrated over the 0.3 TeV to 5 TeV energy range (Cao et al., 2023a), where the corresponding parameters are listed in Table 1. There is a clear agreement between the predicted light curve (solid red line) and the measured energy flux (red dots) for about $T - T_* \sim 3000$ seconds after the GBM trigger, where $T_* = 226$ s is the reference time at the onset of the main component of the afterglow light curves (Cao et al., 2023a).

However, our model's light curve shows an inconsistency with the measured one at early times, $T - T_* \lesssim 10$ s, see solid thin lines. To be specific, the LHAASO-WCDA light curve exhibits an initial rapid rise with a power-law index of approximately 14.9, followed by a slower ascent with a power-law index of roughly 1.82, leading up to its peak value (Cao et al., 2023a). In contrast, our predicted early light curve is less steep than the observed value, see solid red line. One potential explanation for this discrepancy could be the rapid initial rise being influenced by $\gamma\gamma$ attenuation due to the intense prompt photons (e.g., Zhang et al., 2023; Khangulyan et al., 2023). Note a different T_* will give a different rising slope, which could change the above interpretation.

The comoving frame energy density of the prompt photons at the external shocked region can be estimated as

$$u_{\text{GRB}\gamma} \approx L_{\text{GRB}\gamma}^{\text{iso}} / 4\pi R^2 \Gamma^2 c, \quad (17)$$

where $L_{\text{GRB}\gamma}^{\text{iso}}$ represents the isotropic-equivalent gamma ray luminosity. The optical depth to the two-photon annihilation can be approximated as follows (Murase et al., 2022):

$$\begin{aligned} \tau_{\gamma\gamma}^{\text{prompt}} &\approx \sigma_{\gamma\gamma} \frac{R}{\Gamma} \frac{\Gamma u_{\text{GRB}\gamma}}{E_{\text{pk}}} \\ &\approx 220 \frac{\eta_{\gamma\gamma, -1} L_{\text{GRB}\gamma, 53.5}^{\text{iso}}}{R_{16} \Gamma_2^2 E_{\text{pk, MeV}}} \begin{cases} (E_\gamma / \tilde{E}_{\gamma, b})^{\beta-1}, & E_\gamma < \tilde{E}_{\gamma, b} \\ (E_\gamma / \tilde{E}_{\gamma, b})^{\alpha-1}, & E_\gamma > \tilde{E}_{\gamma, b} \end{cases}. \end{aligned} \quad (18)$$

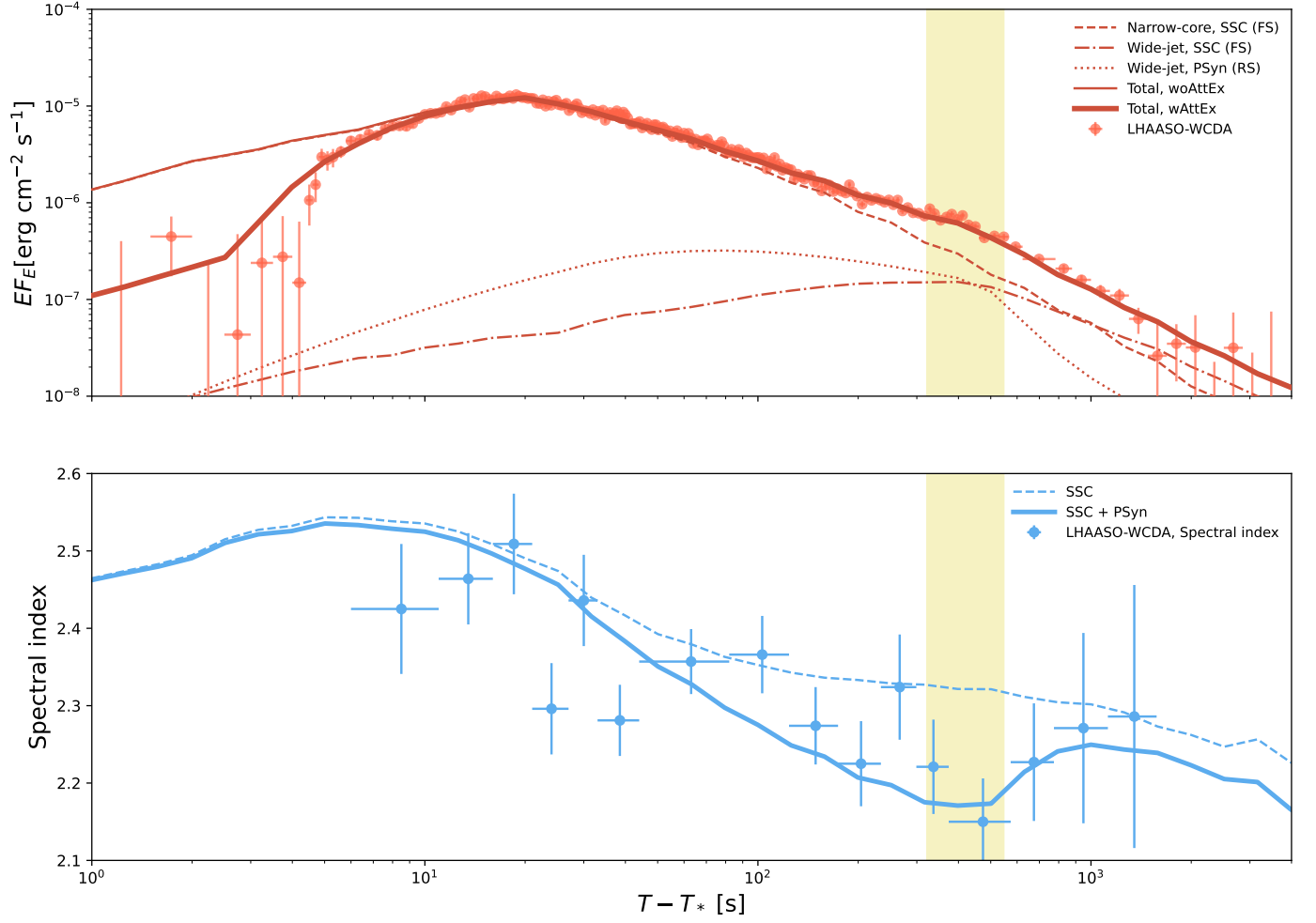


Figure 3: Predicted energy flux (upper panel) and spectral index (lower panel) evolution in the VHE band within the two-component structured jet model. The yellow band indicates the region where there is a small flare.

Here, $\sigma_{\gamma\gamma} \sim \eta_{\gamma\gamma}\sigma_T$ is the $\gamma\gamma$ pair production cross section (Svensson, 1987), σ_T is the Thomson cross section, α and β represent the spectral indices of the prompt emission, $\tilde{E}_{\gamma,b} \approx \Gamma^2 m_e^2 c^4 / E_{\text{pk}} \approx 2.6 \Gamma_{\text{pk,MeV}}^{-1} \text{ GeV}$ denotes the typical energy of high-energy γ -rays that interact with target photons of peak energy E_{pk} in the observer frame (Zhang et al., 2023).

Please note that we are disregarding the anisotropic scattering effect of the beamed prompt photons. In the comoving frame of the external shock region, the direction of VHE gamma rays is isotropically distributed. Despite the monodirectional distribution of prompt target photons, those moving at a large angle relative to the direction of target photons may undergo annihilation. For a distant observer, most of the radiation arrives from the forward direction with $\theta' \lesssim \pi/2$ in the comoving frame, corresponding to $\theta \lesssim 1/\Gamma$ in the observer frame. The anisotropic effect on the attenuation of gamma rays can be estimated via integration over μ' in the comoving frame:

$$\begin{aligned} f_{\text{att}} &= \int_0^1 d\mu' \exp \left[- \int_{\frac{2m_e^2 c^4}{\epsilon'(1-\mu')}} d\epsilon'_t \frac{dn}{d\epsilon'_t} (1-\mu') \sigma_{\gamma\gamma}(\epsilon', \epsilon'_t, \mu') \frac{R}{\Gamma} \right] \\ &\approx \int_0^{\mu'_{\text{th}}} d\mu' \exp[-(1-\mu')\tau_{\gamma\gamma}^{\text{prompt}}] + \int_{\mu'_{\text{th}}}^1 d\mu' \\ &\approx \frac{\exp[-\tau_{\gamma\gamma}^{\text{prompt}}(1-\mu'_{\text{th}})] - \exp[-\tau_{\gamma\gamma}^{\text{prompt}}]}{\tau_{\gamma\gamma}^{\text{prompt}}} + (1-\mu'_{\text{th}}), \quad (19) \end{aligned}$$

where $\tau_{\gamma\gamma}^{\text{prompt}}$ is the optical depth calculated in Eq. 18, ϵ' represents the energy of the gamma rays, ϵ'_t denotes the target photon energy, $dn/d\epsilon'_t$ is the differential target photon number density, μ' is the cosine of the angle between the direction of emitted photons and the direction of prompt target photons in the shock comoving frame and R/Γ represents the comoving frame shock width. Here, μ'_{th} is the cosine of a threshold angle when $E_{\text{pk}}/\Gamma \sim \frac{2m_e^2 c^4}{\epsilon'(1-\mu'_{\text{th}})}$, which depends on the energy of gamma rays and target photon energy. For smaller angles with $\mu' > \mu'_{\text{th}}$, we simply assume that gamma rays can escape freely, considering the threshold energy for two-photon pair annihilation is larger than the peak energy of the prompt emission. For TeV gamma rays with comoving frame energy $\epsilon' \sim 10 \text{ GeV}$ and $E_{\text{pk}}/\Gamma \sim 10 \text{ keV}$, we derive $1 - \mu'_{\text{th}} = 0.005 \lesssim 1/\tau_{\gamma\gamma}^{\text{prompt}}$. Note the value of μ'_{th} is sensitive to both gamma ray energy and Lorentz factor. This demonstrates that attenuation by anisotropic prompt photons leads to a suppression factor proportional to the inverse of the optical depth when $1/\tau_{\gamma\gamma}^{\text{prompt}} \gtrsim 1 - \mu'_{\text{th}}$ and $\tau_{\gamma\gamma}^{\text{prompt}} > 1$, especially for TeV gamma rays.

During the early phase, the jet is in the coasting phase with a Lorentz factor of approximately $\Gamma \approx \Gamma_0$, and the radius of the external shock is approximately $R \approx 2\Gamma_0^2 c(T - T_*)$. For illustrative purposes, we've parameterized the time evolution of the optical depth as

$$\tau_{\gamma\gamma}^{\text{prompt}} = \tau_{\gamma\gamma,0} \left(\frac{T - T_*}{1 \text{ s}} \right)^{-s_\tau}, \quad (20)$$

where $\tau_{\gamma\gamma,0} \simeq 180$ and $s_\tau = 3$. The value of $\tau_{\gamma\gamma,0}$ is estimated using the parameters $L_{\text{GRB}\gamma} = 10^{54} \text{ erg s}^{-1}$, $R = 10^{15.4} \text{ cm}$ and $\Gamma = 400$. In this context, we assume that $L_{\text{GRB}\gamma}^{\text{iso}} \propto$

$(T - T_*)^{-2}$ and that $R \propto (T - T_*)$ during the early afterglow phase. The prompt emission flux in the 20 keV - 10 MeV range is $1.62 \times 10^{-2} \text{ erg cm}^{-2} \text{ s}^{-1}$ during the time interval $T_0 + [225.024 - 233.216] \text{ s}$ and $3.15 \times 10^{-4} \text{ erg cm}^{-2} \text{ s}^{-1}$ during the time interval $T_0 + [241.408 - 249.600] \text{ s}$ (Frederiks et al., 2023). The energy flux decreases by two orders of magnitude when the VHE gamma ray light curve reaches its peak. The observed flux in the VHE band, after accounting for the $\gamma\gamma$ attenuation by the prompt photons, can be obtained as,

$$EF_E = EF_E|_{\text{woAttEx}} f_{\text{att}}, \quad (21)$$

where $EF_E|_{\text{woAttEx}}$ is the flux without considering the attenuation by external prompt photons. The attenuation factor for gamma rays with observed energies exceeding 300 GeV is $f_{\text{att}} \sim 0.08$, gradually increasing to unity at later times. Therefore, we attribute the rapid increase in early TeV afterglow data to the effect of $\gamma\gamma$ attenuation by the prompt photons, see the solid thick line in Fig. 3, which is consistent with the observed data and aligns with the argument presented in (Khangulyan et al., 2023; Shen et al., 2023). Note that the reference time T_* is uncertain, and a larger T_* results in a shallower slope in the early light curve.

The energy flux in the VHE band peaks around $T - T_* \sim 18 \text{ s}$, which is consistent with the jet's duration, approximately $\delta T_{\text{ej}} \sim 10 \text{ s}$. Following the peak, the energy flux decreases over time, displaying a power-law spectral index of about 1.1, consistent with the findings reported by Cao et al. (2023a). It was also noted in Cao et al. (2023a) that the sharp decline in flux around $T - T_* \sim 670 \text{ s}$ aligns with the jet break, resulting in an energy flux decreases with a power-law index of approximately 2.2. In our study, we propose an alternative explanation. We suggest that the steep drop in the light curve is caused by the emission from the wide jet (depicted as a red dotted-dash curve), while the jet break in the emission from the narrow core occurred earlier. Furthermore, there's a small flare around $T - T_* = [320, 550] \text{ s}$ as reported in (Cao et al., 2023a). In our model, the emergence of reverse shock proton synchrotron emission (illustrated as a red dotted curve) appears to coincide with this observed flare.

3.2. Spectral hardening and reverse shock proton synchrotron emission

In the lower panel of Fig. 3, we compare the predicted spectral index evolution with the observed data, where the spectral index is defined as $EF_E \propto E^{-s+2}$. We notice a subtle trend in the spectral index as time progresses Cao et al. (2023a). Initially, during the rising phase at $T - T_* \sim 10 - 20 \text{ s}$, it's relatively soft at around 2.4. As the time elapses, it gradually decreases, reaching a minimum spectral index of approximately 2.2 at $T - T_* \sim 400 \text{ s}$. Afterward, it starts to become softer again, with a spectral index of around ~ 2.3 at $T - T_* \sim 1000 \text{ s}$. We observed that the spectral index evolution of the SSC component from the narrow jet does not match the measured values where the spectral index gradually decreases from 2.4 to 2.3, as shown by the dashed curve. Remarkably, the observed change in spectral index finds a straightforward explanation with the

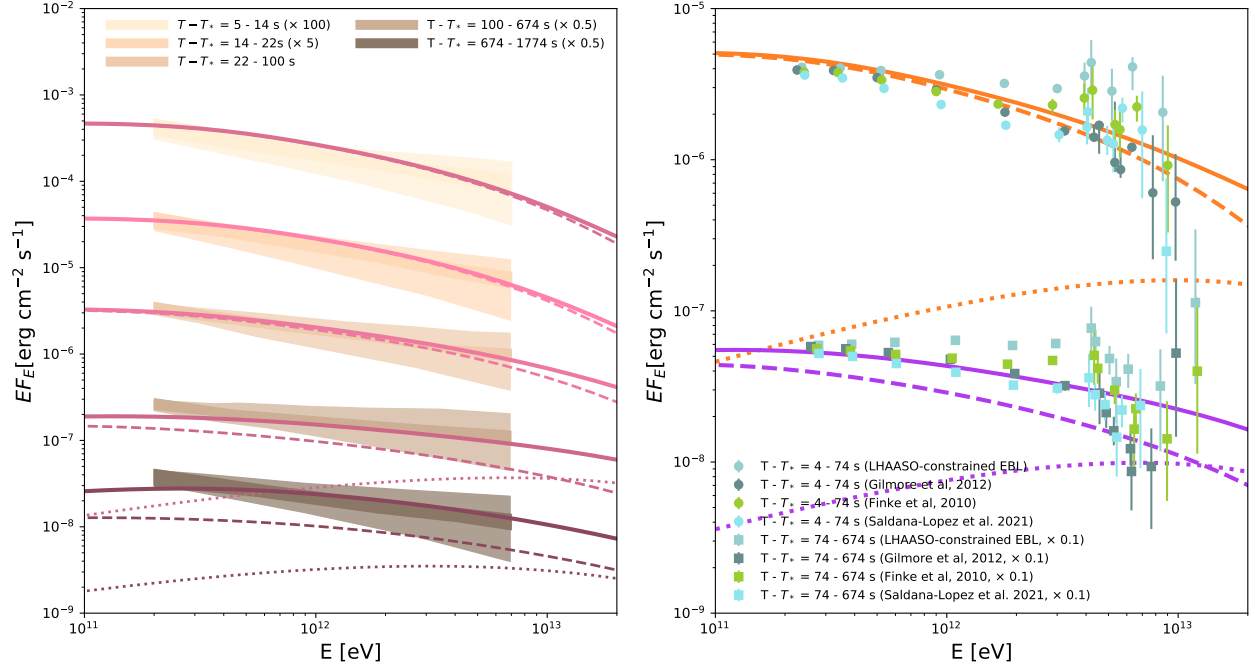


Figure 4: The expected VHE gamma ray energy spectrum from GRB 221009A during the afterglow phase. The dashed lines depict SSC radiation from the forward shock of the narrow core, while dotted lines show proton synchrotron emission from the reverse shock of the wide jet. In the left panel, we compare our theoretical model with the measured energy spectra from LHAASO-WCDA, which go up to 7 TeV. The measurements have been adjusted using an EBL model (Saldana-Lopez et al., 2021; Cao et al., 2023a). The inner bands represent statistical uncertainties, and the outer bands indicate systematic uncertainties. In the right panel, we compare the intrinsic energy spectra after correction for various EBL models, including data from LHAASO-KM2A (Cao et al., 2023b).

Table 1: Physical parameters adopted in this work.

Parameter	Narrow-core	Wide-Jet
$\mathcal{E}_k[\text{erg}]$	4×10^{55}	3×10^{55}
Γ_0	430	400
$n_{\text{ex},0}[\text{cm}^{-3}]$	300	300
A_*	1	1
k	2	2
$\delta T_{\text{ej}}[\text{s}]$	10	400(3000)
$\theta_j[\text{deg}]$	0.12	5.7
$\theta_c[\text{deg}]$	-	0.0005
a	-	2
$\theta_v[\text{deg}]$	0	0
ϵ_B	3×10^{-4}	1.5×10^{-4}
ϵ_e	0.008	0.0022
f_e	0.25	0.008
s_e	2.3	2.3
ϵ_B^r	-	0.5
ϵ_e^r	-	0.002
f_e^r	-	0.008
s_e^r	-	2.4
ϵ_p^r	-	0.25
s_p^r	-	2

^a $\delta T_{\text{ej}} = 3000$ s when $\theta_j > 1.1$ deg.

^b $\epsilon_B^r = 0.1$ when $\theta_j > 1.1$ deg.

introduction of an additional component: the reverse shock proton synchrotron emission. The energy spectral index of this proton synchrotron emission is $(s_p^r + 1)/2 = 3/2$ for $s_p^r = 2$, which is significantly harder compared to the inverse-Compton spectral index in the TeV energy range (e.g., Zhang et al., 2023). The reduced Chi-square is $\chi^2/\text{d.o.f.} = 3.3$ by the SSC model curve and it is $\chi^2/\text{d.o.f.} = 2.8$ with reverse shock proton synchrotron emission as an additional component. We also performed a Kolmogorov-Smirnov (KS) test to determine which model, SSC or SSC + Psyn, is more consistent with the spectral index evolution. The distribution of normalized residuals for each model is calculated based on the 16 data points shown in the lower panel of Fig. 3. We create a histogram with a range from -3.5 to 3.5 and a bin size of 0.5. We find the p-value of the KS test with only the SSC component (1.5×10^{-3}) is smaller than the model including the reverse shock proton synchrotron emission as a second component (1.1×10^{-2}), which means the latter gives a better fit to the data. Note the results are affected by the limited number of data points. However, because of the computation cost, this work does not aim to find the best-fit parameters that match the observed light curves and spectra. We notice that the spectral index's shift towards harder values aligns well with the peak time of the proton synchrotron emission. Furthermore, this change in spectral behavior correlates with the emergence of a flare at $T - T_* = [320, 550]$ s (Cao et al., 2023a).

In Fig. 4, we show the calculated energy spectrum in the early phase ($T - T_* < 2000$ s) of the VHE band, taking into account $\gamma\gamma$ attenuation by prompt photons as in Eq. 21. What we see

is that the primary source of the observed flux is the SSC emission from the narrow core. Furthermore, the later spectral hardening observed can be attributed to the reverse shock proton synchrotron emission from the wide jet.

Next, we'll analytically estimate the proton synchrotron emission from the reverse shock at the time of shock crossing, referred to as T_\times . To do this, we assume that the duration of the GRB ejecta, measured in the stellar frame, is $\delta T_{\text{ej}} = 100$ s. The width of the ejecta, measured in the stellar frame, can be approximated as:

$$\Delta_0 \approx c\delta T_{\text{ej}} \approx 3 \times 10^{12} \delta T_{\text{ej},2} \text{ cm.} \quad (22)$$

We can estimate the jet spreading radius as

$$R_s \approx \Delta_0 \Gamma_0^2 \approx 3 \times 10^{17} \delta T_{\text{ej},2} \text{ cm.} \quad (23)$$

The deceleration radius is

$$R_{\text{dec}} \approx 8.4 \times 10^{16} \mathcal{E}_{54.5}^{1/3} \Gamma_{0,2.5}^{-2/3} n_{\text{ex},2}^{-1/3} \text{ cm.} \quad (24)$$

Under the condition $R_s > R_{\text{dec}}$, the ejecta is in the thick shell case. The radius at which the reverse shock crosses is approximately,

$$R_\times \approx 6.4 \times 10^{16} \mathcal{E}_{54.5}^{1/4} \delta T_{\text{ej},2}^{1/4} n_{\text{ex},2}^{-1/4} \text{ cm.} \quad (25)$$

At the time $T_\times = \delta T_{\text{ej}}$, the Lorentz factor of the shocked ejecta is

$$\Gamma_\times \approx 86 \mathcal{E}_{54.5}^{1/8} \delta T_{\text{ej},2}^{-3/8} n_{\text{ex},2}^{-1/8}. \quad (26)$$

The relative Lorentz factor of the shocked ejecta, when measured in the unshocked ejecta frame, is

$$\Gamma_{34} \approx 1.9. \quad (27)$$

The number density of the unshocked ejecta in the comoving frame can be calculated as

$$\begin{aligned} n_{\text{ej}} &= \frac{\mathcal{E}_k}{4\pi m_p c^2 \Gamma_0 (\Gamma_0 \Delta_0) R_\times^2} \\ &= 2.5 \times 10^5 \mathcal{E}_{54.5}^{1/2} \Gamma_{0,2.5}^{-2} \delta T_{\text{ej},2}^{-3/2} n_{\text{ex},2}^{1/2} \text{ cm}^{-3}. \end{aligned} \quad (28)$$

The magnetic field strength can be determined as follows,

$$\begin{aligned} B_\times &= (32\pi \epsilon_B' \Gamma_{34} n_{\text{ej}} (\Gamma_{34} - 1) m_p c^2)^{1/2} \\ &\approx 135 \epsilon_{B,-0.5}^{r1/2} \mathcal{E}_{54.5}^{1/4} \Gamma_{0,2.5}^{-1} \delta T_{\text{ej},2}^{-3/4} n_{\text{ex},2}^{1/4} (g(\Gamma_{34})/2.4)^{1/2} \text{ G,} \end{aligned} \quad (29)$$

where $g(\Gamma_{34}) \equiv (\Gamma_{34} - 1)(\Gamma_{34} + 3/4)$. In the comoving frame, the acceleration timescale is estimated to be $t_{\text{acc}} = \eta \epsilon_{p,\text{max}} / (eB)$, and the dynamical timescale is $t_{\text{dyn}} = R_\times / (c\beta \Gamma_\times)$. The maximum proton energy measured in the stellar frame under the confinement condition $t_{\text{acc}} < t_{\text{dyn}}$ can be estimated as,

$$\begin{aligned} E_{p,\text{max}}^{\text{dyn}} &\approx \Gamma_\times \epsilon_{p,\text{max}} \approx \eta^{-1} \Gamma_\times e B_\times (R_\times / \Gamma_\times) \\ &\approx 2.7 \times 10^{21} \eta^{-1} \epsilon_{B,-0.5}^{r1/2} \mathcal{E}_{54.5}^{1/4} \Gamma_{0,2.5}^{-1} \delta T_{\text{ej},2}^{-3/4} \left(\frac{g(\Gamma_{34})}{2.4} \right)^{1/2} \text{ eV,} \end{aligned} \quad (30)$$

where η is a coefficient which is a few in the Bohm limit (e.g., Sironi et al., 2015). The maximum energy is limited by the synchrotron cooling process, and we find,

$$\begin{aligned} E_{p,\text{max}}^{\text{syn}} &= \sqrt{\frac{6\pi e}{\sigma_T B_\times \eta Z^3} \frac{m_p^2 c^2}{m_e}} \Gamma_\times \\ &\approx 1.4 \times 10^{21} \eta^{-1/2} Z^{-3/2} \epsilon_{B,-0.5}^{r-1/4} \\ &\times \Gamma_{0,2.5}^{-1/2} n_{\text{ex},2}^{-1/4} \left(\frac{g(\Gamma_{34})}{2.4} \right)^{-1/4} \text{ eV.} \end{aligned} \quad (31)$$

The maximum energy of protons is then given by

$$E_{p,\text{max}} = \min[E_{\text{max}}^{\text{dyn}}, E_{\text{max}}^{\text{syn}}]. \quad (32)$$

The flux of the proton synchrotron emission, which peaks at the maximum energy $E_{\text{psyn}} = \Gamma_\times \epsilon_\gamma = \min[\Gamma_\times \epsilon_{\text{psyn},M}, \Gamma_\times \epsilon_{\text{psyn},c}]$, can be expressed as

$$F_E = \frac{1+z}{4\pi d_L^2} N_3(E_{p,\text{max}}) P_E, \quad (33)$$

Here, $N_3(E_{p,\text{max}})$ represents the number of protons, and P_E is the laboratory frame specific synchrotron power per proton,

$$\begin{aligned} P_E &\approx \frac{\phi_0 \sqrt{3} e^3}{m_p c^2} B_\times \Gamma_\times \\ &\approx 1.5 \times 10^{-21} \text{ erg s}^{-1} \text{ Hz}^{-1}, \end{aligned} \quad (34)$$

where ϕ_0 is a factor of order unity. The typical energy of the proton synchrotron emission in the observer frame is given by

$$\begin{aligned} E_M^{\text{psyn}} &\approx \frac{3}{4\pi} \frac{he B_\times}{m_p c} \gamma_{p,\text{max}}^2 \Gamma_\times / (1+z) \\ &\approx 3.5 \times 10^{13} / (1+z) \text{ eV,} \end{aligned} \quad (35)$$

where $\gamma_{p,\text{max}} = (E_{p,\text{max}} / \Gamma_\times) / m_p c^2$ is the maximum Lorentz factor of protons. The cooling energy is determined by the balance between synchrotron cooling timescale and dynamical timescale. The proton cooling energy is estimated to be $E_{p,c} \approx 5.6 \times 10^{20}$ eV and the corresponding characteristic photon energy is

$$\begin{aligned} E_c^{\text{psyn}} &\approx \frac{3}{4\pi} \frac{he B_\times}{m_p c} \gamma_{p,c}^2 \Gamma_\times / (1+z) \\ &\approx 5.8 \times 10^{12} / (1+z) \text{ eV,} \end{aligned} \quad (36)$$

where $\gamma_{p,c} = (E_{p,c} / \Gamma_\times) / m_p c^2$ is the cooling Lorentz factor of protons. It is important to note that the peak of the proton synchrotron emission in the EF_E spectrum occurs at $\min[E_c^{\text{psyn}}, E_M^{\text{psyn}}]$.

The comoving frame energy density of nonthermal protons can be calculated as

$$\int_{\epsilon_{p,\text{min}}}^{\epsilon_{p,\text{max}}} d\epsilon_p \epsilon_p \frac{dn}{d\epsilon_p} = \epsilon_p' e_3 = 4\epsilon_p' \Gamma_{34} (\Gamma_{34} - 1) n_{\text{ej}} m_p c^2, \quad (37)$$

where $\varepsilon_{p,\min} \sim \Gamma_{34} m_p c^2$. The total number density of nonthermal protons is given by

$$n_{p,3} = \int_{\varepsilon_{p,\min}}^{\varepsilon_{p,\max}} d\varepsilon_p \frac{dn}{d\varepsilon_p}. \quad (38)$$

The number of protons at $E_{p,\max}$ can be estimated as

$$\begin{aligned} N_3(E_{p,\max}) &\approx 4\pi R_\times^2 \Delta_\times \varepsilon_p \left. \frac{dn}{d\varepsilon_p} \right|_{\varepsilon_p = \varepsilon_{p,\max}} \\ &\approx 4\pi R_\times^2 \Delta_\times \frac{\epsilon_p^t 4\Gamma_{34}(\Gamma_{34} - 1) n_{ej} m_p c^2}{\ln(\varepsilon_{p,\max}/\varepsilon_{p,\min}) \varepsilon_{p,\max}} \\ &\approx 1.5 \times 10^{43}, \end{aligned} \quad (39)$$

assuming $s_p^r = 2$ and $\epsilon_p^r = 0.6$. Finally, we can derive the differential flux estimated at E_m as

$$EF_E|_{E=E_m} \approx 3.2 \times 10^{-6} \text{ erg cm}^{-2} \text{ s}^{-1}. \quad (40)$$

We can see the estimated flux is consistent with Fig. 3 and Fig. 4. Note that the above analytical estimates neglect adiabatic cooling of accelerated protons and internal $\gamma\gamma$ attenuation, which are considered in the numerical calculations. Considering that adiabatic cooling reduces the proton synchrotron flux by approximately a factor of 2, and gamma-rays with energies $\gtrsim 10$ TeV are further suppressed by an additional factor of a few due to internal $\gamma\gamma$ attenuation.

3.3. Late-time afterglow and reverse shock emission

In Fig. 5, we compare the predicted multi-wavelength light curve with the observed flux across a wide range of energy bands, from radio to VHE.

Early on, roughly within the first 10^3 s, the energy flux is mainly attributed to the external forward shock emission from the narrow jet. However, at later times, beyond approximately $10^3 - 10^4$ s, the dominant contribution to the energy flux shifts to the external forward shock emission from the wide jet. This transition is highlighted in the left panel of Fig. 5.

In the right panel, we further analyze the energy flux evolution in the lower energy range compared to the observed flux, spanning from radio to optical bands. Around $T - T_* = 10^4$ s, the energy flux in the optical bands is primarily governed by the external forward shock synchrotron emission from the wide jet. However, in the radio band, the external forward shock synchrotron emission from the narrow core dominates the energy flux until around $T - T_* = 10^4$ s, when the wide jet's emission takes over.

In Fig. 6, we compare the reverse shock electron synchrotron emission from the wide jet to the observed data in the low-energy radio to optical bands. Although it's not as prominent as the forward shock emission, unlike the reverse shock emission, the forward shock light curve is expected to remain relatively constant in the case of a wind medium, which aligns with the findings presented in Gill and Granot (2023). They considered emission from a shallow angular structured jet similar to our wide jet component in the thick shell scenario (Gill and Granot, 2023). Similar to Gill and Granot (2023); Zheng et al.

(2023); Ren et al. (2023), we found that the reverse shock emission from the wide jet is considerably higher than the forward shock emission at $T \sim 10^4$ s which could account for the observed bump at $\sim 10 - 20$ GHz (Bright et al., 2023; Gill and Granot, 2023; Zheng et al., 2023; Ren et al., 2023). Note the two bumps on the reverse shock emission are related to the duration of the ejecta, which is $\delta T_{ej} = 400$ s for $\theta < 1.1^\circ$ and $\delta T_{ej} = 3000$ s for $\theta > 1.1^\circ$. It's important to note that photons from the reverse shock electron synchrotron emission play a significant role as they can impact the escape of VHE photons above 10 TeV, which are generated through proton synchrotron emission.

4. Discussion and implications

4.1. VHE gamma rays from GRBs

In our analysis, we thoroughly investigate the two primary sources of VHE gamma rays in GRB 221009A: SSC emission and proton synchrotron emission. Here's what we found:

- For the SSC process, our calculations reveal that narrow-core SSC emission dominates the early TeV afterglow, while the wide-jet SSC emission takes over in the later stages.
- Proton synchrotron emission becomes most significant during the transition phase around $T - T_0 \sim 600$ s, where the reverse shock finishes crossing the ejecta of the wide jet. Although the proton synchrotron component doesn't dominate the entire VHE band light curve, it plays a crucial role during this critical period.

A closer examination of the VHE spectral index reveals an intriguing pattern: the VHE spectra start soft, then become hard, and finally steepen in the late stages. This evolution trend is challenging to explain within the standard SSC model alone. It seems more natural to introduce an additional component responsible for spectral hardening. The proton synchrotron component offers a plausible explanation because it inherently produces harder spectral indices, see Sec. 4.2 for caveats. Note that similar behavior of spectral hardening at late time has also been observed in GRB 190829A, which is difficult to explain within the standard SSC model (Abdalla et al., 2019; Huang et al., 2023a). The reverse shock proton synchrotron component discussed in this work could be helpful to alleviate the limitation of the standard SSC model.

In this work, we employ a two-component jet model to explain the VHE gamma rays observed by LHAASO. As demonstrated in Section 3.3, the wide-jet component is necessary to account for the late-time radio to optical data. Specifically, the reverse shock radio emission from the wide-jet component aligns with the observed optically thick rising radio light curve.

The model parameters we found for the wide-jet component are very similar to those adopted in Ref. Gill and Granot (2023). For example, the isotropic equivalent kinetic energy \mathcal{E}_k , A_* , and ϵ_B are around 2 times larger than those in Ref. Gill and Granot (2023). Our value of ϵ_e is 2 times smaller. The power-law index of the energy angular profile $a = 2$ is larger than the

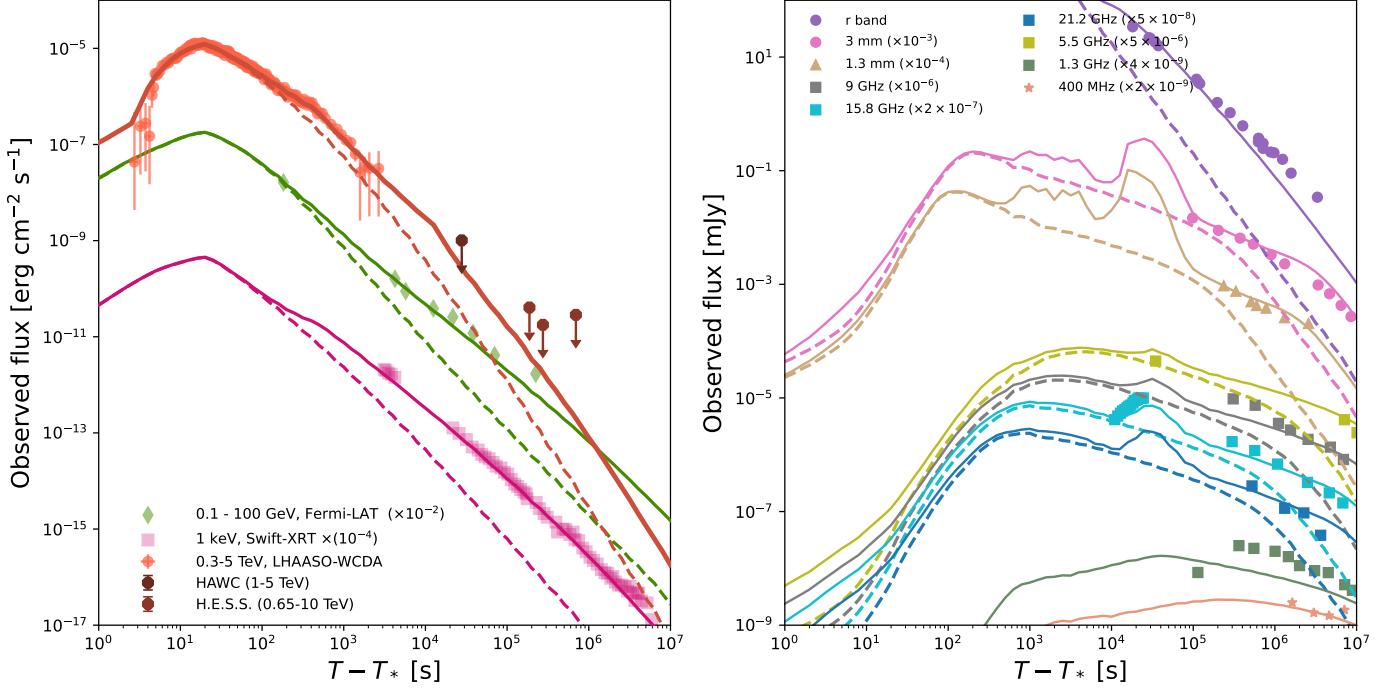


Figure 5: Predicted afterglow light curve for GRB 221009A across multiple wavelengths. The solid lines represent the combined emission from both the narrow core and wide jet, while the dashed lines depict the contributions from the narrow core alone. Light curves for radio, millimeter, optical, and X-ray are taken from (Laskar et al., 2023; O'Connor et al., 2023; Bright et al., 2023). The optical data is corrected for extinction. The *Fermi*-LAT light curve is obtained from (Bissaldi et al., 2023), and the TeV light curve is obtained from (Cao et al., 2023a). Upper limits in the VHE band from H.E.S.S. (Aharonian et al., 2023) and HAWC (Ayala and HAWC Collaboration, 2022) are included.

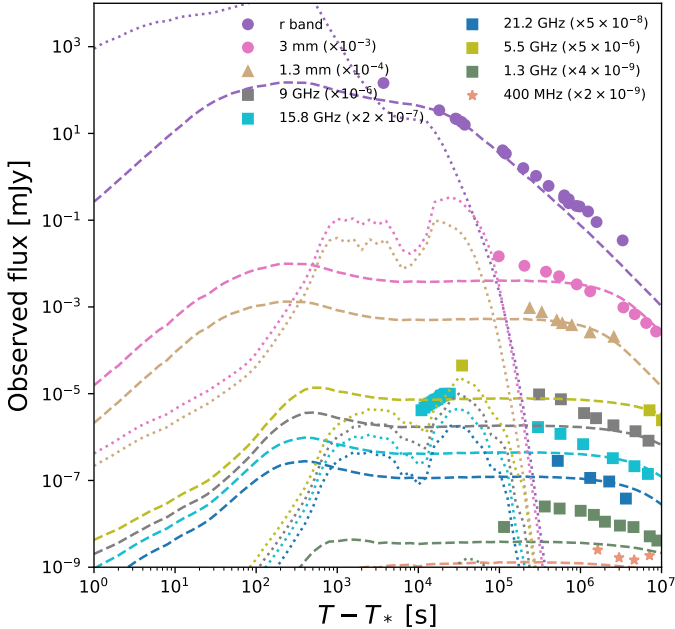


Figure 6: Similar to Fig. 5, we compare the reverse-forward shock emission from the wide jet to the observed data in the low-energy radio to optical bands. The dashed lines represent the external forward shock emission, while the dotted lines represent the external reverse shock emission.

value $a \sim 0.8$ found in Ref. Gill and Granot (2023). However, Ref. Gill and Granot (2023) only conducted fitting to the late-time radio to X-ray band, aligning with our results. Based on Fig.3, we found that the SSC emission from the wide-jet (dotted-dashed line) cannot explain the TeV light curve, contributing significantly only at late time $T - T_0 \sim 1000$ seconds. Thus, the observed TeV light curve needs to be explained with another jet component, e.g., the narrow-core (e.g., Cao et al., 2023a). In comparison to the model parameters adopted in Ref. Cao et al. (2023a), the width of the narrow core is slightly narrower, with $\theta_j \sim 0.22$ degrees. This narrower jet is necessary to avoid overshooting the late-time radio data. Our calculations suggest that the change in the decaying slope of the light curve is attributed to the emergence of the wide-jet component.

Both work from Ref. Zheng et al. (2023) and Ref. Ren et al. (2023) performed multiwavelength fitting up to the TeV band for GRB 221009A, considering a two-component structured jet model. However, both the model details and the values of physical parameters differ. The isotropic equivalent energy of the wide-jet component we found is over ~ 1 order of magnitude more energetic than Ref. Zheng et al. (2023), but consistent with Ref. Ren et al. (2023). Compared to Ref. Zheng et al. (2023) and Ref. Ren et al. (2023), our model is more consistent with the light curve at 100 GHz band. We found that the observed X-ray flux around 3000 seconds is dominated by the wide-jet component, which is underpredicted in Ref. Ren et al. (2023). Finally, we should note that our model involves the reverse shock proton synchrotron emission in addition to the

SSC component, providing a better description of the TeV light curve and energy spectrum measured by LHAASO.

4.2. Remarks on proton synchrotron radiation

Proton synchrotron emission has been proposed as one of the mechanisms to produce high-energy emission from GRBs Totani (1998a,b); Zhang and Meszaros (2001); Kumar and Zhang (2014). The maximum photon energy produced by high-energy electrons is $E_{\text{syn,e}} \sim 50\Gamma/(1+z)$ MeV, while it is $E_{\text{syn,p}} \sim 10^2\Gamma/(1+z)$ GeV for protons. Given the typical Lorentz factor of the outflow, $\Gamma \sim 100$, the maximum energy of proton synchrotron emission could reach $E_{\text{syn,p}} \sim 10\Gamma_2/(1+z)$ TeV. High-energy electron SSC radiation provides a natural explanation for VHE gamma rays, where low-energy seed photons are scattered to the VHE energy range Meszaros and Rees (1994); Dermer et al. (2000); Sari and Esin (2001); Zhang and Meszaros (2001). However, SSC radiation undergoes Klein-Nishina suppression, which makes it challenging to explain the gamma ray spectrum above 10 TeV and the hard spectra index. Thus, proton synchrotron emission are considered as one of the possible mechanisms to produce VHE gamma rays.

For a given energy, the energy loss rate for protons is smaller by a factor of $(m_e/m_p)^4$ than for electrons, where m_e is electron mass and m_p is proton mass Zhang (2018). Due to the low efficiency, proton synchrotron emission may require an unreasonably large luminosity to explain *Fermi*-LAT GRBs above 100 MeV Crumley and Kumar (2013). Explaining TeV light curves is less demanding but a large fraction of energy needs to be carried nonthermal protons with $\epsilon_p \lesssim 1$ considering forward shock proton synchrotron emission Isravel et al. (2023b,a).

The reverse shock proton synchrotron emission undergoes a similar issue mentioned above but with the advantage of stronger magnetic fields. From Eqs. (33) and (34), we see that the proton synchrotron emission flux prefers higher magnetic field strength and a larger number of high-energy protons. We adopt a spectral index of $s_p^r = 2$ for protons accelerated by the reverse shock. Our results indicate that $\epsilon_p^r \sim 30\%$ of ejecta internal energy is transferred to nonthermal protons and $\epsilon_B^r \sim 60\%$ is converted to magnetic energy. Note there is parameter degeneracy, if the magnetic field is stronger, the energy fraction by protons is smaller. Our model also required the acceleration of protons to be very efficient near the Bohm limit with $\eta \sim 1-10$. We can see the required parameter range is different from the standard ones Kumar and Zhang (2014).

In this work, we simply adopt the basic requirement, $\epsilon_p^r + \epsilon_B^r + \epsilon_e^r \lesssim 1$, to constrain the proton synchrotron emission in our model. We consider weakly magnetized shocks in matter-dominated jets, where particle acceleration and the generation of magnetic fields could be efficient Sironi et al. (2015), and rather optimistic values of these parameters are still allowed. For nonrelativistic collisionless shocks, $\epsilon_p^r \sim 10-20\%$ is inferred from hybrid particle-in-cell (PIC) simulations (Caprioli and Spitkovsky, 2014). Ref. Crumley et al. (2019) conducted kinetic simulations of mildly relativistic shocks and discovered a linear increase in energy consistent with Bohm scaling, and exceeds the rate at ultrarelativistic shocks (Sironi et al., 2013). Note the PIC simulations are only available for a limited time

and length scales, and the long-term evolution is necessary to unveil details (Groselj et al., 2024). The value of ϵ_B^r depends on the properties of the upstream. The upstream may have $\sigma_{\text{mag,ej}} < 1$ where $\sigma_{\text{mag,ej}}$ is the ejecta magnetization, but after the shock compression, the value of ϵ_B^r could be greater than 0.1 while the ejecta is still matter-dominated Zhang and Kobayashi (2005). A larger ϵ_B^r in the reverse shock region than the forward shock region has been revealed from modeling of some previous GRBs such as GRB 990123 (see Ref. Zhang et al. (2003)) and other GRBs that showed a dominant RS emission in the optical band Yi et al. (2020).

Here, we discuss several situations where the extreme values of the parameters mentioned above could be alleviated. Recent studies have revealed that as a reverse shock moves through a magnetized jet with a large-scale cylindrical magnetic field, particles undergo curvature drift and escape upon reaching the confinement limit. This process leads to a significantly harder spectral index of $s \sim 1$ (e.g., Huang et al., 2023b). By adopting such a hard spectral index of $s_p^r = 1$, we find that converting $\sim 10\%$ of ejecta internal energy into nonthermal protons with an equal amount into the magnetic field energy is sufficient to explain the observed flux of VHE gamma rays above 10 TeV, potentially alleviating the efficiency issue. In addition, we assume microphysical parameters such as ϵ_B^r are homogeneous in the shocked region, but the inhomogeneity in both number density and magnetic field strength can be relevant and could effectively enhance the synchrotron radiation power (Groselj et al., 2024). Due to such model uncertainties, the final flux could vary by a factor of 2. Given this uncertainty, optimistic values of the parameters are still possible, and future high-resolution simulations incorporating long-term evolution are necessary to further explore the feasibility of efficient acceleration, especially in the context of mildly relativistic, magnetized, electron-ion shocks.

Although proton synchrotron emission requires parameters different from the usual ones, these parameters are still allowed in this event as mentioned above, and hence the proton synchrotron model is undoubtedly an interesting possibility for this event. In the future, high-resolution simultaneous observations of the energy spectrum from the GeV to the TeV band are essential to constrain the peak energy and curvature of the SSC spectrum, and a hard spectrum above the peak energy of the SSC spectrum supports proton synchrotron emission.

4.3. Ultrahigh-energy neutrinos from GRBs

In this section, we present the expected flux of high-energy neutrinos from the reverse shock proton synchrotron model. The GRB afterglow is expected to emit PeV-EeV neutrinos via the photomeson production process (Waxman and Bahcall, 2000; Dermer, 2002; Li et al., 2002; Murase, 2007; Razzaque, 2013). However, there is no evidence of a correlation between neutrinos and GRBs analyzed with candidate muon-neutrino events observed by IceCube (Abbasi et al., 2022; Lucarelli et al., 2023). Abbasi et al. (2022) found the total contributions to the quasi-diffuse neutrino flux is less than 24%

for an emission timescale 10^4 seconds. The detection of PeV-EeV neutrinos would require future UHE neutrino telescopes such as GRAND 200k (Álvarez-Muñiz et al., 2020), IceCube-Gen2 (Abbasi et al., 2021), RNO-G (Aguilar et al., 2021), as well as POEMMA (Venters et al., 2020).

The neutrino fluence can be approximated as (e.g., Murase et al., 2022; Kimura, 2022)

$$E_\nu^2 \phi_{\nu_\mu} \approx \frac{1}{8} \frac{1+z}{4\pi d_L^2} \min[1, f_{p\gamma}] f_{\text{sup}} \mathcal{E}_{\text{cr}} \frac{1}{\mathcal{R}_{\text{cr}}} \\ \simeq 5.4 \times 10^{-1} \min[1, f_{p\gamma}] f_{\text{sup}} \text{ GeV cm}^{-2}, \quad (41)$$

where $f_{p\gamma}$ is the effective optical depth of the photomeson production process with the reverse shock synchrotron emission as the main target photon fields, f_{sup} is the suppression factor by pion and muon cooling, $\mathcal{E}_{\text{cr}} = \epsilon_p^r 4\pi R_\times^2 \Delta_\times e_3 \Gamma_\times \sim 8 \times 10^{54}$ erg is the isotropic-equivalent cosmic ray proton energy accelerated by reverse shock, and $\mathcal{R}_{\text{cr}} = \ln(\epsilon_{p,\text{max}}/\epsilon_{p,\text{min}}) \simeq 23$ converts the bolometric cosmic ray energy to the differential cosmic ray energy. In Fig. 7, we show the predicted single flavor neutrino fluence in the reverse shock proton synchrotron model, which are numerically calculated with Eq. 6 by integrating over the emission time with $T \sim 10^7$ seconds. At the peak energy, the corresponding photomeson production efficiency is estimated to be $f_{p\gamma} \lesssim 0.1$ at the shock crossing time. For comparison purposes, we also present the neutrino fluence expected in the forward shock model, assuming a fraction of $\epsilon_p = 0.1$ of the post-shock thermal energy goes into high-energy protons and protons could be accelerated to ultrahigh energies. The accelerated protons follow a power-law distribution with spectral index $s_p = 2$. We can see that the predicted neutrino fluence peaked at the ultra-high-energy range and is lower than the 90% C.L. upper limits by IceCube. Even though the neutrino flux from a single GRB is undetectable, the diffuse neutrino flux contributed from all GRBs could provide valuable tests of the model (Murase, 2007).

4.4. GRBs as UHECR sources

In this study, we examined proton synchrotron emission from protons accelerated to ultra-high energies. We estimated that the total energy of these accelerated nonthermal protons is approximately $\mathcal{E}_{\text{cr}} \sim 8 \times 10^{54}$ erg. However, detecting escaping UHECR protons from GRBs simultaneously with VHE gamma rays is challenging. UHECR undergoes various energy loss processes during the journey to Earth (e.g., Waxman, 1995; Vietri, 1996). The influence of magnetic fields within both host galaxies and extragalactic space can not be neglected. These magnetic fields can introduce significant time delays in the arrival of UHECRs compared to the rectilinear propagation scenario (e.g., Miralda-Escudé and Waxman, 1996; Murase and Takami, 2009). Note that the magnetic field in our galaxy also deflects the arrival direction of UHECRs and causes significant time delays, as shown in Murase and Takami (2009). A recent study suggested that a UHECR burst from GRB 221009A could be detected within about 10 years if inter-galactic magnetic fields with strength $\lesssim 10^{-13}$ G (He et al., 2024). However, in our scenario, we consider UHECRs escaping directly from

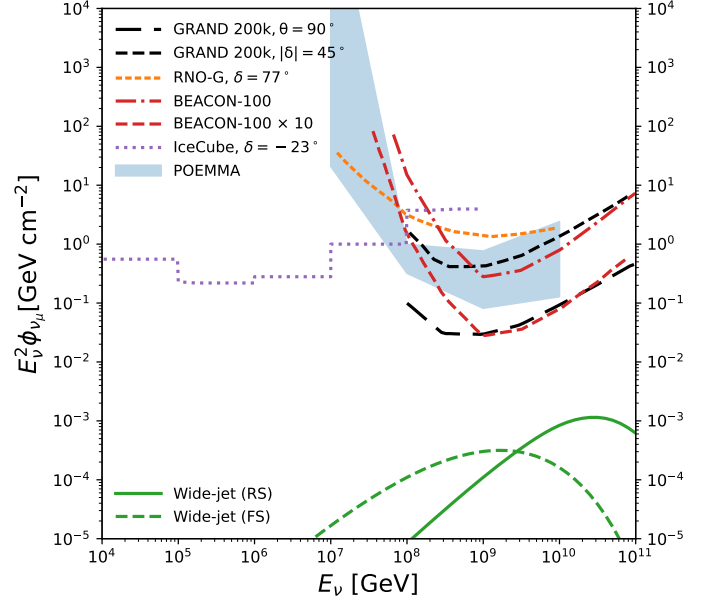


Figure 7: Neutrino fluence predicted in the reverse shock proton synchrotron model for wide-jet. For comparison purposes, we also present the neutrino fluence expected in the forward shock model, assuming a fraction of $\epsilon_p = 0.1$ of the post-shock thermal energy goes into high-energy protons. We show the sensitivity of GRAND for a source at declination $\delta = 45^\circ$ and zenith angle $\theta = 90^\circ$ (Álvarez-Muñiz et al., 2020), RNO-G at $\delta = 77^\circ$ (Aguilar et al., 2021), IceCube at $\delta = -23^\circ$ (Abbasi et al., 2021), BEACON (Zeolla et al., 2023), and POEMMA taking the 90% unified confidence level and assuming observations during astronomical night (Venters et al., 2020).

the source, with neutron escape playing an insignificant role. Consequently, we predict a lower flux of UHECRs from GRBs compared to the estimates in He et al. (2024). Furthermore, the combined effects of magnetic fields within galaxies and large-scale structures (Takami and Murase, 2012), and energy losses during intergalactic propagation significantly complicate the detection of such emissions. Additionally, the UHECR-induced intergalactic electromagnetic cascades could also generate VHE gamma rays (Alves Batista, 2022; Das and Razaque, 2023; Mirabal, 2022). However, the time delay and the development of the electromagnetic cascades strongly depend on the structure and strength of intergalactic magnetic fields (Murase et al., 2012), which require further investigation.

5. Summary

In this study, we conducted a comprehensive investigation of radiation within the standard external reverse-forward shock scenario, considering a two-component structured jet comprising a narrow core dominated by magnetic energy and a wide jet dominated by matter. We compared our numerical findings with observed energy spectra and multi-wavelength light curves spanning from radio to VHE bands. Our key results are summarized as follows:

- The energy flux light curve observed in the VHE band is primarily dominated by SSC emission from the narrow core. The SSC emission from the wide jet only

becomes dominant at late times, approximately beyond 10^3 seconds. Reverse shock proton synchrotron emission becomes significant when the reverse shock crosses the shocked ejecta of the wide jet around $T - T_0 \sim 600$ seconds, coinciding with the emergence of a mild flare around $T - T_0 \sim [546, 776]$ seconds after the trigger.

- The initial rapid rise of the VHE band light curve is due to $\gamma\gamma$ attenuation caused by prompt target photons, although the reference time T_* is uncertain, and a different T_* changes the early light curve significantly.
- Compared to the inverse-Compton process, reverse shock proton synchrotron emission exhibits a much harder spectrum in the VHE band. This naturally explains the observed energy spectrum hardening and potentially contributes significantly to the photon flux above $\gtrsim 10$ TeV.
- The multi-wavelength afterglow light curve from radio to the GeV band can be explained within the two-component structured jet model. The emission from the wide jet starts to dominate the observed multi-wavelength afterglow after $T - T_0 \sim 10^3 - 10^4$ seconds, while radio emission from the narrow core may continue to dominate the flux at even later times, until around $T - T_0 \sim 10^4$ seconds. The reverse shock emission from the wide jet could explain the steep rise of the ~ 10 GHz radio data at $T - T_0 \sim 10^4$ seconds.
- Our findings may support the idea that GRBs are efficient accelerators of UHECRs, especially at the reverse shock. Further multimessenger observations involving more events are essential to better understand the energy budget of UHECRs originating from GRBs.

acknowledgments

The work of K.M. is supported by the NSF grants Nos. AST-2108466, AST-2108467, and AST-2308021. It is also supported by KAKENHI Nos. 20H01901 and 20H05852 (B.T.Z. and K.M.), and No. 22H00130, 20H01901, 20H00158, 23H05430, 23H04900 (K.I.). We acknowledge support by Institut Pascal at Université Paris-Saclay during the Paris-Saclay Astroparticle Symposium 2023, with the support of the P2IO Laboratory of Excellence (program “Investissements d’avenir” ANR-11-IDEX-0003-01 Paris-Saclay and ANR-10-LABX-0038), the P2I axis of the Graduate School of Physics of Université Paris-Saclay, as well as IJCLab, CEA, IAS, OS-UPS, and the IN2P3 master projet UCMN (B.T.Z.).

Appendix A. Numerical modeling of nonthermal radiation from the external reverse-forward shock

Appendix A.1. Dynamics

When ultra-relativistic ejecta of the GRB propagate into the external medium, the ejecta are decelerated as their kinetic energy is transferred to the external medium. Two shocks are formed: a forward shock advancing into the ambient external

Unshocked ejecta	Shocked ejecta	Shocked external medium	Unshocked external medium
Γ_4	$\Gamma_3 = \Gamma_2$	Γ_2	$\Gamma_1 = 1$
	$p_3 = p_2$	p_2	
n_{ej}	$n_3 = 4\Gamma_{34}n_{ej}$	$n_2 = 4\Gamma_{21}n_{ex}$	n_{ex}
	$e_3 = n_3(\Gamma_{34} - 1)m_p c^2$	$e_2 = n_2(\Gamma_{21} - 1)m_p c^2$	
	$u_e^r = \epsilon_e^r e_3$	$u_e = \epsilon_e e_2$	
	$u_p^r = \epsilon_p^r e_3$	$u_p = \epsilon_p e_2$	
	$u_B^r = \epsilon_B^r e_3$	$u_B = \epsilon_B e_2$	
RS		CD	FS

Figure A.8: Notations and shock jump conditions for the reverse-forward shock system.

medium, and a reverse shock moving backward in the ejecta rest frame, as illustrated in Fig. A.8.

Following the method proposed in Nava et al. (2013); Zhang (2018), we incorporate the influence of the reverse shock on the dynamical evolution of the outflow. We solve the following differential equations,

$$\frac{d\Gamma}{dR} = -\frac{(\Gamma_{\text{eff},2} + 1)(\Gamma - 1)c^2 \frac{dm}{dR} + \Gamma_{\text{eff},2} \frac{d\mathcal{E}'_{\text{ad},2}}{dR}}{(M_{\text{ej},3} + m)c^2 + \mathcal{E}'_{\text{int},2} \frac{d\Gamma_{\text{eff},2}}{d\Gamma} + \mathcal{E}'_{\text{int},3} \frac{d\Gamma_{\text{eff},3}}{d\Gamma}} - \frac{(\Gamma - \Gamma_0 - \Gamma_{\text{eff},3} + \Gamma_{\text{eff},3}\gamma_{34})c^2 \frac{dM_{\text{ej},3}}{dR} + \Gamma_{\text{eff},3} \frac{d\mathcal{E}'_{\text{ad},3}}{dR}}{(M_{\text{ej},3} + m)c^2 + \mathcal{E}'_{\text{int},2} \frac{d\Gamma_{\text{eff},2}}{d\Gamma} + \mathcal{E}'_{\text{int},3} \frac{d\Gamma_{\text{eff},3}}{d\Gamma}}, \quad (\text{A.1})$$

where

$$\Gamma_{\text{eff},2} \equiv (\hat{\gamma}\Gamma^2 - \hat{\gamma} + 1)/\Gamma, \quad (\text{A.2})$$

in needed to properly describe the Lorentz transformation of the internal energy, and the corresponding adiabatic index is $\hat{\gamma} = (4\Gamma + 1)/3\Gamma$. When calculating $\Gamma_{\text{eff},3}$, we use $\hat{\gamma} = (4\Gamma_{34} + 1)/3\Gamma_{34}$ where $\Gamma_{34} = \Gamma\Gamma_0(1 - \beta\beta_0)$ represents the relative Lorentz factor between the shocked and unshocked ejecta. Note parameters with \prime represent comoving frame value.

The mass of the unshocked ejecta that completes crossing the reverse shock is given by:

$$\frac{dM_{\text{ej},3}}{dR} = \frac{M_{\text{ej}}}{cT_{\text{ej}}} \frac{\beta_0 - \beta}{\beta}. \quad (\text{A.3})$$

The evolution of the internal energy of the shocked external matter can be determined by the differential equation,

$$\frac{d\mathcal{E}'_{\text{int},2}}{dR} = (1 - \epsilon_\gamma)(\Gamma - 1)4\pi R^2 n_{\text{ex}} m_p c^2 + \frac{d\mathcal{E}'_{\text{ad},2}}{dR}, \quad (\text{A.4})$$

where ϵ_γ represents the radiation efficiency. The evolution of the adiabatic energy of the shocked external medium is described by the equation:

$$\frac{d\mathcal{E}'_{\text{ad},2}}{dR} = -(\hat{\gamma} - 1) \left(\frac{3}{R} - \frac{1}{\Gamma} \frac{d\Gamma}{dR} \right) \mathcal{E}'_{\text{int},2}. \quad (\text{A.5})$$

The evolution of the internal energy of the shocked ejecta can be determined by the following differential equation

$$\frac{d\mathcal{E}'_{\text{int},3}}{dR} = (\Gamma_{34} - 1) \frac{dM_{\text{ej},3}}{dR} c^2 + \frac{d\mathcal{E}'_{\text{ad},3}}{dR}. \quad (\text{A.6})$$

The evolution of the adiabatic energy of the shocked ejecta is given by

$$\frac{d\mathcal{E}'_{\text{ad},3}}{dR} = -(\hat{\gamma} - 1) \left(\frac{3}{R} - \frac{1}{\Gamma} \frac{d\Gamma}{dR} \right) \mathcal{E}'_{\text{int},3}. \quad (\text{A.7})$$

Once the reverse shock finishes crossing the ejecta, the evolution of the shocked ejecta follows the power law scaling $\Gamma \propto R^{-g}$, with $g = 2$ in the thin shell case and $g = 7/2$ in the thick shell case (Kobayashi, 2000). The evolution of the blastwave radius is given by

$$\frac{dR}{dt} = \beta c, \quad (\text{A.8})$$

where $\beta = \sqrt{1 - 1/\Gamma^2}$. The evolution of the jet angular width is

$$\frac{d\theta_j}{dR} = \frac{c_s}{\Gamma R c}, \quad (\text{A.9})$$

where c_s is the speed of sound. Note in this work, the lateral expansion of the jet is not taken into account (Zhang and MacFadyen, 2009).

Appendix A.2. Radiative processes

Appendix A.2.1. Particle acceleration and cooling

Based on the diffusive shock acceleration mechanism, the accelerated particles, including both electrons and ions, are assumed to follow a power law distribution with an exponential cutoff with the maximum momentum,

$$\dot{n}_p^{\text{inj}} = C p^{-s} \exp(-p/p_{\text{max}}) \quad (p > p_{\text{inj}}), \quad (\text{A.10})$$

where p_{inj} is the comoving frame injection momentum, p_{max} is the comoving frame maximum momentum, s is the spectral index. The downstream internal energy density in the shocked external medium is

$$e_2 = (\Gamma_{21} - 1) n_2 m_p c^2 = (\Gamma_{21} - 1) 4\Gamma_{21} n_1 m_p c^2, \quad (\text{A.11})$$

where $\Gamma_{21} = \Gamma$ is the relative Lorentz factor. The normalization constant C is constrained with following equation,

$$t_{\text{dyn}} \int dp \dot{n}_p^{\text{inj}} = n_2. \quad (\text{A.12})$$

We also assume particles are injected at a constant rate within the dynamical time. The comoving frame dynamical timescale is

$$t_{\text{dyn}} \approx R/\Gamma\beta c. \quad (\text{A.13})$$

The acceleration timescale is parameterized as

$$t_{\text{acc}} = \eta t_L = \eta \frac{p}{ZeBc}, \quad (\text{A.14})$$

and the maximum acceleration momentum is given by

$$p_{\text{max,dyn}} = \frac{1}{\eta} \frac{R}{\Gamma\beta} ZeB. \quad (\text{A.15})$$

The synchrotron cooling timescale is

$$t_{\text{syn}}^{-1} = \frac{\sigma_T Z^4 m_e^2 B^2}{6\pi m^4 c^3} p. \quad (\text{A.16})$$

The maximum acceleration is limited by synchrotron cooling

$$p_{\text{max,syn}} = \sqrt{\frac{1}{\eta} \frac{6\pi e}{\sigma_T Z^3 B} \frac{m^2 c^2}{m_e}}, \quad (\text{A.17})$$

and we have

$$p_{\text{max}} = \min[p_{\text{max,dyn}}, p_{\text{max,syn}}]. \quad (\text{A.18})$$

For electrons, the minimum injection momentum of the non-thermal electrons is

$$p_{e,\text{inj}} = [(\epsilon_{e,\text{kin}} + m_e c^2)^2 - m_e^2 c^4]^{1/2}, \quad (\text{A.19})$$

where

$$\epsilon_{e,\text{kin}} = \frac{\epsilon_e}{f_e} g(s_e) (\Gamma - 1) m_p c^2, \quad (\text{A.20})$$

and

$$g(s_e) \approx \begin{cases} \frac{s_e - 2}{s_e - 1}, & s_e > 2 \\ \ln^{-1} \left(\frac{p_{e,\text{max}}}{p_{e,\text{inj}}} \right), & s_e = 2 \end{cases}. \quad (\text{A.21})$$

Note that Eq. A.19-A.20 are also valid in the nonrelativistic case, which is essential for late-time afterglow modeling. For protons, the minimum injection energy is assumed to be thermal energy, then the minimum injection momentum is estimated to be

$$p_{p,\text{inj}} \approx [((\Gamma - 1) m_p c^2 + m_p c^2)^2 - m_p^2 c^4]^{1/2} = (\Gamma^2 - 1)^{1/2} m_p c^2. \quad (\text{A.22})$$

The particle distribution function per unit volume, $n_p = \partial n / \partial p$, is determined by solving the following kinetic equation (e.g., Blumenthal and Gould, 1970; Zhang et al., 2021a; Derishev and Piran, 2021)

$$\frac{n_p}{\partial t} = -\frac{\partial}{\partial p} (\dot{p} n_p) - \dot{n}_p^{\text{inj}} - \frac{n_p}{t_{\text{exp}}} - \frac{n_p}{t_{\text{esc}}}, \quad (\text{A.23})$$

where \dot{n}_p^{inj} is the particle injection rate, t_{exp} is the expansion time of the shocked region, t_{esc} is the possible escape time,

$$\dot{p} \equiv \frac{dp}{dt} = p t_{\text{cool}}^{-1} = p [t_{\text{syn}}^{-1}(p) + t_{\text{IC}}^{-1}(p) + t_{\text{ad}}^{-1}], \quad (\text{A.24})$$

is the particle cooling rate, including synchrotron energy losses, inverse-Compton cooling, and adiabatic cooling. We determine the particle distribution with the iteration method (Murase et al., 2011; Zhang et al., 2021a),

$$n_p = \frac{1}{t_{\text{cool}}^{-1} + t_{\text{dyn}}^{-1}} \frac{1}{p} \int_{p_{\text{eff}}}^{\infty} dp' \dot{n}_p^{\text{inj}}(p'). \quad (\text{A.25})$$

In Ref. Derishev and Piran (2021), the term $1/t_{\text{eff}} = 1/t_{\text{esc}} + 1/t_{\text{exp}}$ is treated as the effective particle lifetime. In this work, we consider the maximum particle lifetime as t_{dyn} . In the slow cooling case, Eq. A.25 gives a reasonably good approximation of the particle energy spectrum derived through numerically solving the time-dependent kinetic equation. In the fast-cooling regime, Eq. A.25 gives the steady-state solution (See Eq. C.3 in Dermer and Menon, 2009). In addition, we adopt

$$p_{\text{eff}} = \frac{p_{\text{inj}} p_{\text{cool}}}{p_{\text{inj}} + p_{\text{cool}}}, \quad (\text{A.26})$$

as the effective particle momentum determined by particle injection momentum p_{inj} and cooling momentum p_{cool} , which gives a better approximation to the particle distribution when $p_{\text{inj}} \sim p_{\text{cool}}$. We can observe that $p_{\text{eff}} \approx p_{\text{inj}}$ when $p_{\text{inj}} \ll p_{\text{cool}}$, and $p_{\text{eff}} \approx p_{\text{cool}}$ when $p_{\text{inj}} \gg p_{\text{cool}}$. For protons, gives that $p_{\text{inj}} \ll p_{\text{cool}}$, we have $p_{\text{eff}} \approx p_{\text{inj}}$. The dynamical timescale, measured in the comoving frame, is defined as

$$t_{\text{dyn}} = \int \frac{dR}{\Gamma \beta c}. \quad (\text{A.27})$$

Due to the expansion of the emitting region, particles undergo adiabatic energy losses, and the energy lost rate is estimated to be (e.g., Dermer and Menon, 2009)

$$\left| \frac{dp_e}{dR} \right|_{\text{ad}} = \frac{p_e}{R} \left(1 - \frac{1}{3} \frac{d \ln \Gamma}{d \ln R} \right), \quad (\text{A.28})$$

and the corresponding adiabatic cooling timescale can be estimated as

$$t_{\text{ad}} = \left(\frac{1}{p_e} \left| \frac{dp_e}{dR} \right|_{\text{ad}} \frac{dR}{dt} \right)^{-1} = \frac{R}{\Gamma \beta c} \left(1 - \frac{1}{3} \frac{R}{\Gamma} \frac{d \Gamma}{d R} \right)^{-1}. \quad (\text{A.29})$$

The expansion time of the shocked region is $t_{\text{exp}} = V/\dot{V} = R/3\dot{R} = t_{\text{ad}}/3$ (Gould, 1975; Derishev and Piran, 2021). The synchrotron cooling timescale is given by Eq. A.16. The inverse-Compton cooling timescale of nonthermal electrons can be approximated as

$$t_{\text{IC}}^{-1} = \frac{1}{\varepsilon_e} \left| \frac{d\varepsilon_e}{dt} \right|_{\text{IC}} \approx \frac{4}{3} \sigma_{\text{TC}} \frac{\varepsilon_e}{m_e^2 c^4} u_{\text{ph}}(\varepsilon_\gamma) F_{\text{KN}}, \quad (\text{A.30})$$

where F_{KN} is a factor to take into account the Klein-Nishina effect.

The synchrotron emissivity can be calculated using Eq. C3 in Zhang et al. (2021a). Note there is a typo in Eq. C3, where an additional term ε' in the denominator is unnecessary. The numerical calculation is not affected. The formula used in AMES is

$$j_{\varepsilon_\gamma}^{\text{syn}} = \frac{\sqrt{3}}{4\pi} \frac{e^3 B}{m_e c^2 2\pi \hbar} \int d\gamma_e n_{\gamma_e} G(x), \quad (\text{A.31})$$

where

$$G(x) \approx \frac{1.81 e^{-x}}{(x^{-2/3} + (3.62/\pi)^2)^{1/2}}, \quad (\text{A.32})$$

$x = \varepsilon_\gamma/\varepsilon_c$, and $\varepsilon_c = (3e\hbar B/2m_e c)\gamma_e^2 \beta^2$ is the critical energy.

The comoving SSC emissivity is calculated with Eq. C5 in Zhang et al. (2021a). Note the comoving-frame target synchrotron photon density is estimated as

$$\frac{dn^{\text{syn}}}{d\varepsilon_\gamma} = 4\pi j_{\varepsilon_\gamma}^{\text{syn}} \times t_{\text{esc}}, \quad (\text{A.33})$$

where $t_{\text{esc}} \approx 2w/c$ is the photon escape timescale and w is the width of the shocked shell estimated in Eq. 8. The factor of 2 takes into account the geometrical effect when photons escape from a thin shell (Fukushima et al., 2017; Derishev and Piran, 2019).

Appendix A.2.2. Emission from reverse shock

The total number of protons (or electrons) in the ejecta shell is given by

$$N_{0,4} = \frac{\mathcal{E}_k}{\Gamma_0 m_p c^2}, \quad (\text{A.34})$$

where Γ_0 is the initial Lorentz factor and \mathcal{E}_k is the isotropic-equivalent kinetic energy. The comoving frame number density of the unshocked ejecta is given by

$$n_4(R) = \frac{N_{0,4}}{4\pi R^2 \Gamma_0 \Delta_0} = \frac{\mathcal{E}_k}{4\pi m_p c^2 \Gamma_0 (\Gamma_0 \Delta_0) R^2}, \quad (\text{A.35})$$

where Δ_0 is the initial width of the ultra-relativistic ejecta shell that represents the geometrical thickness measured in the laboratory frame. It is defined as

$$\Delta_0 = \max \left[c t_{\text{ej}}/(1+z), \frac{R}{2\Gamma_0^2} \right], \quad (\text{A.36})$$

where $R/2\Gamma_0^2$ represents the shell width due to the radial spreading of the ejecta.

The comoving frame number density of protons (or electrons) in the shocked ejecta is given by

$$n_3 = 4\Gamma_{34} n_4, \quad (\text{A.37})$$

where

$$\Gamma_{34} = \frac{1}{2} \left(\frac{\Gamma_0}{\Gamma} + \frac{\Gamma}{\Gamma_0} \right). \quad (\text{A.38})$$

The total number of protons (or electrons) in the shocked ejecta shell can be estimated as

$$N_3 = N_{0,4} \frac{M_{\text{ej},3}}{M_{\text{ej}}}. \quad (\text{A.39})$$

The comoving frame width of the shocked ejecta shell can be estimated as

$$\Delta_3 = \frac{N_3}{4\pi R^2 n_3}. \quad (\text{A.40})$$

Then, we can estimate the value of Δs as

$$\Delta s = \frac{\Delta_3}{\Gamma|\mu - \beta_{\text{sh}}|}. \quad (\text{A.41})$$

The downstream internal energy density is given by

$$e_3 = (\Gamma_{34} - 1) n_3 m_p c^2. \quad (\text{A.42})$$

The downstream magnetic field strength is

$$B_3 = (8\pi\epsilon_{B,r}e_3)^{1/2}. \quad (\text{A.43})$$

The minimum electron energy is

$$\epsilon_{m,e} = g(s_{e,r}) \frac{\epsilon_{e,r}}{f_{e,r}} (\Gamma_{34} - 1) \frac{m_p}{m_e} m_e c^2, \quad (\text{A.44})$$

where $g(s_{e,r}) = (s_{e,r} - 2)/(s_{e,r} - 1)$ for $s_{e,r} > 2$, and $s_{e,r}$ is the nonthermal electron spectral index in the reverse shock region. The maximum electron energy is

$$\epsilon_{M,e} = \left(\frac{6\pi e}{\sigma_T B_3 \eta_r} \right)^{1/2} m_e c^2, \quad (\text{A.45})$$

where η_r is a parameter that describes the details of acceleration, with a typical value of around a few in the Bohm limit. Similar to the forward shock, we determine the nonthermal electron distribution with Eq. A.25 before the reverse shock finishes crossing the ejecta.

In the post RS-crossing phase, we adopt a parameterized power law decay of the shocked ejecta

$$\Gamma_3 \propto r^{-g}, \quad (\text{A.46})$$

where $g = 7/2$ in the thick shell case and $g = 2$ in the thin shell case (Kobayashi, 2000; Zhang, 2018). Note that the total number of protons (or electrons) remains constant,

$$N_3 = N_{0,4}. \quad (\text{A.47})$$

In the thick shell case, the evolution of the comoving frame energy density is given by

$$e_3 = e_3(t_\times) \left(\frac{R}{R_\times} \right)^{-26/3}, \quad (\text{A.48})$$

and the number density is

$$n_3 = n_3(t_\times) \left(\frac{R}{R_\times} \right)^{-13/2}. \quad (\text{A.49})$$

The evolution of the magnetic field is given by

$$B_3 = B_3(t_\times) \left(\frac{R}{R_\times} \right)^{-13/3}. \quad (\text{A.50})$$

Additionally, the evolution of the comoving frame width is

$$\Delta_3 = \Delta_3(t_\times) \left(\frac{R}{R_\times} \right)^{9/2}. \quad (\text{A.51})$$

In the thin shell case, the evolution of the energy density is

$$e_3 = e_3(t_\times) \left(\frac{R}{R_\times} \right)^{-8(3+g)/7}, \quad (\text{A.52})$$

and the number density is

$$n_3 = n_3(t_\times) \left(\frac{R}{R_\times} \right)^{-6(3+g)/7}, \quad (\text{A.53})$$

The evolution of the magnetic field is given by

$$B_3 = B_3(t_\times) \left(\frac{R}{R_\times} \right)^{-4(3+g)/7}. \quad (\text{A.54})$$

Additionally, the evolution of the comoving frame width is

$$\Delta_3 = \Delta_3(t_\times) \left(\frac{R}{R_\times} \right)^{6(3+g)/7-2}. \quad (\text{A.55})$$

References

- Abbasi, R., et al. (IceCube-Gen2), 2021. Sensitivity studies for the IceCube-Gen2 radio array. *PoS ICRC2021*, 1183. doi:10.22323/1.395.1183, arXiv:2107.08910.
- Abbasi, R., et al. (IceCube, Fermi Gamma-ray Burst Monitor), 2022. Searches for Neutrinos from Gamma-Ray Bursts Using the IceCube Neutrino Observatory. *Astrophys. J.* 939, 116. doi:10.3847/1538-4357/ac9785, arXiv:2205.11410.
- Abbasi, R., et al. (IceCube), 2023. Limits on Neutrino Emission from GRB 221009A from MeV to PeV Using the IceCube Neutrino Observatory. *Astrophys. J. Lett.* 946, L26. doi:10.3847/2041-8213/acc077, arXiv:2302.05459.
- Abbott, B.P., et al. (LIGO Scientific, Virgo), 2017a. GW170817: Observation of Gravitational Waves from a Binary Neutron Star Inspiral. *Phys. Rev. Lett.* 119, 161101. doi:10.1103/PhysRevLett.119.161101, arXiv:1710.05832.
- Abbott, B.P., et al. (LIGO Scientific, Virgo, Fermi GBM, INTEGRAL, IceCube, AstroSat Cadmium Zinc Telluride Imager Team, IPN, Insight-Hxmt, ANTARES, Swift, AGILE Team, 1M2H Team, Dark Energy Camera GW-EM, DES, DLT40, GRAWITA, Fermi-LAT, ATCA, ASKAP, Las Cumbres Observatory Group, OzGrav, DWF (Deeper Wider Faster Program), AST3, CAASTRO, VINROUGE, MASTER, J-GEM, GROWTH, JAGWAR, CaltechNRAO, TTU-NRAO, NuSTAR, Pan-STARRS, MAXI Team, TZAC Consortium, KU, Nordic Optical Telescope, ePESSTO, GROND, Texas Tech University, SALT Group, TOROS, BOOTES, MWA, CALET, IKI-GW Follow-up, H.E.S.S., LOFAR, LWA, HAWC, Pierre Auger, ALMA, Euro VLBI Team, Pi of Sky, Chandra Team at McGill University, DFN, ATLAS Telescopes, High Time Resolution Universe Survey, RIMAS, RATIR, SKA South Africa/MeerKAT), 2017b. Multi-messenger Observations of a Binary Neutron Star Merger. *Astrophys. J. Lett.* 848, L12. doi:10.3847/2041-8213/aa91c9, arXiv:1710.05833.
- Abdalla, H., et al., 2019. A very-high-energy component deep in the γ -ray burst afterglow. *Nature* 575, 464–467. doi:10.1038/s41586-019-1743-9, arXiv:1911.08961.
- Abdalla, H., et al. (H.E.S.S.), 2021. Revealing x-ray and gamma ray temporal and spectral similarities in the GRB 190829A afterglow. *Science* (New York, N.Y.) 372, 1081–1085. doi:10.1126/science.abe8560, arXiv:2106.02510.
- Acciari, V.A., et al. (MAGIC), 2019a. Observation of inverse Compton emission from a long γ -ray burst. *Nature* 575, 459–463. doi:10.1038/s41586-019-1754-6, arXiv:2006.07251.
- Acciari, V.A., et al. (MAGIC), 2019b. Teraelectronvolt emission from the γ -ray burst GRB 190114C. *Nature* 575, 455–458. doi:10.1038/s41586-019-1750-x, arXiv:2006.07249.
- Acciari, V.A., et al. (MAGIC), 2021. MAGIC Observations of the Nearby Short Gamma-Ray Burst GRB160821B. *Astrophys. J.* 908, 90. doi:10.3847/1538-4357/abd249, arXiv:2012.07193.
- Aguilar, J.A., et al. (RNO-G), 2021. Design and Sensitivity of the Radio Neutrino Observatory in Greenland (RNO-G). *JINST* 16, P03025. doi:10.1088/1748-0221/16/03/P03025, arXiv:2010.12279. [Erratum: *JINST* 18, E03001 (2023)].
- Aharonian, F., et al. (H.E.S.S.), 2023. H.E.S.S. Follow-up Observations of GRB 221009A. *Astrophys. J. Lett.* 946, L27. doi:10.3847/2041-8213/acc405, arXiv:2303.10558.
- Ai, S., Gao, H., 2023. Model Constraints Based on the IceCube Neutrino Nondetection of GRB 221009A. *Astrophys. J.* 944, 115. doi:10.3847/1538-4357/acb3bf, arXiv:2210.14116.

- Álvarez-Muñiz, J., et al. (GRAND), 2020. The Giant Radio Array for Neutrino Detection (GRAND): Science and Design. *Sci. China Phys. Mech. Astron.* 63, 219501. doi:10.1007/s11433-018-9385-7, arXiv:1810.09994.
- Alves Batista, R., 2022. GRB 221009A: a potential source of ultra-high-energy cosmic rays. arXiv e-prints, arXiv:2210.12855doi:10.48550/arXiv.2210.12855, arXiv:2210.12855.
- Asano, K., Inoue, S., Mészáros, P., 2009. PROMPT HIGH-ENERGY EMISSION FROM PROTON-DOMINATED GAMMA-RAY BURSTS. *The Astrophysical Journal* 699, 953–957. URL: <https://iopscience.iop.org/article/10.1088/0004-637X/699/2/953>, doi:10.1088/0004-637X/699/2/953.
- Asano, K., Murase, K., Toma, K., 2020. Probing Particle Acceleration through Broadband Early Afterglow Emission of MAGIC Gamma-Ray Burst GRB 190114C. *The Astrophysical Journal* 905, 105. doi:10.3847/1538-4357/abc82c.
- Ayala, H., HAWC Collaboration, 2022. GRB 221009A: Upper limits from HAWC 8 hours after trigger. *GRB Coordinates Network* 32683, 1.
- Bissaldi, E., Bruel, P., Omodei, N., Pillera, R., Di Lalla, N., 2023. GRB 221009A: The brightest burst of all time as seen by Fermi-LAT. *PoS ICRC2023*, 847. doi:10.22323/1.444.0847.
- Blanch, O., Gaug, M., Noda, K., Berti, A., Moretti, E., Miceli, D., Gliwny, P., Ubach, S., Schleicher, B., Cerruti, M., Stamerra, A., MAGIC Collaboration, 2020a. MAGIC observations of GRB 201015A: hint of very high energy gamma-ray signal. *GRB Coordinates Network* 28659, 1.
- Blanch, O., Longo, F., Berti, A., Fukami, S., Suda, Y., Loporchio, S., Miccanovic, S., Green, J.G., Pinter, V., Takahashi, M., MAGIC Collaboration, 2020b. GRB 201216C: MAGIC detection in very high energy gamma rays. *GRB Coordinates Network* 29075, 1.
- Blumenthal, G.R., Gould, R.J., 1970. Bremsstrahlung, Synchrotron Radiation, and Compton Scattering of High-Energy Electrons Traversing Dilute Gases. *Reviews of Modern Physics* 42, 237–270. doi:10.1103/RevModPhys.42.237.
- Bright, J.S., et al., 2023. Precise measurements of self-absorbed rising reverse shock emission from gamma-ray burst 221009A. *Nature Astron.* 7, 986–995. doi:10.1038/s41550-023-01997-9, arXiv:2303.13583.
- Burns, E., Svinkin, D., Fenimore, E., Kann, D.A., Agüí Fernández, J.F., Frederiks, D., Hamburg, R., Lesage, S., Temiraev, Y., Tsvetkova, A., Bissaldi, E., Briggs, M.S., Dalessi, S., Dunwoody, R., Fletcher, C., Goldstein, A., Hui, C.M., Hristov, B.A., Kocovski, D., Lysenko, A.L., Mailyan, B., Mangan, J., McBreen, S., Racusin, J., Ridnaia, A., Roberts, O.J., Ulanov, M., Veres, P., Wilson-Hodge, C.A., Wood, J., 2023. GRB 221009A: The BOAT. *The Astrophysical Journal Letters* 946, L31. doi:10.3847/2041-8213/acc39c.
- Cao, Z., et al. (LHAASO), 2023a. A tera-electron volt afterglow from a narrow jet in an extremely bright gamma-ray burst. *Science* 380, adg9328. doi:10.1126/science.adg9328, arXiv:2306.06372.
- Cao, Z., et al. (LHAASO), 2023b. Very high energy gamma-ray emission beyond 10 TeV from GRB 221009A. *Sci. Adv.* 9, adj2778. doi:10.1126/sciadv.adj2778, arXiv:2310.08845.
- Caprioli, D., Spitkovsky, A., 2014. Simulations of Ion Acceleration at Non-relativistic Shocks. I. Acceleration Efficiency. *Astrophys. J.* 783, 91. doi:10.1088/0004-637X/783/2/91, arXiv:1310.2943.
- Crumley, P., Caprioli, D., Markoff, S., Spitkovsky, A., 2019. Kinetic simulations of mildly relativistic shocks – I. Particle acceleration in high Mach number shocks. *Mon. Not. Roy. Astron. Soc.* 485, 5105–5119. doi:10.1093/mnras/stz232, arXiv:1809.10809.
- Crumley, P., Kumar, P., 2013. Hadronic Models for LAT Prompt Emission Observed in Fermi Gamma-Ray Bursts. *Mon. Not. Roy. Astron. Soc.* 429, 3238. doi:10.1093/mnras/sts581, arXiv:1210.7802.
- Das, S., Razzaque, S., 2023. Ultrahigh-energy cosmic-ray signature in GRB 221009A. *Astron. Astrophys.* 670, L12. doi:10.1051/0004-6361/202245377, arXiv:2210.13349.
- Derishev, E., Piran, T., 2019. The Physical Conditions of the Afterglow Implied by MAGIC's Sub-TeV Observations of GRB 190114C. *Astrophys. J. Lett.* 880, L27. doi:10.3847/2041-8213/ab2d8a, arXiv:1905.08285.
- Derishev, E., Piran, T., 2021. GRB Afterglow Parameters in the Era of TeV Observations: The Case of GRB 190114C. *The Astrophysical Journal* 923, 135. doi:10.3847/1538-4357/ac2dec.
- Dermer, C.D., 2002. Neutrino, neutron, and cosmic ray production in the external shock model of gamma-ray bursts. *Astrophys. J.* 574, 65–87. doi:10.1086/340893, arXiv:astro-ph/0005440.
- Dermer, C.D., Chiang, J., Mitman, K.E., 2000. Beaming, baryon-loading, and the synchrotron self-compton component in gamma-ray burst blast waves energized by external shocks. *Astrophysical Journal* 537, 785. doi:10.1086/309061, arXiv:astro-ph/9910240.
- Dermer, C.D., Menon, G., 2009. *High Energy Radiation from Black Holes: Gamma Rays, Cosmic Rays, and Neutrinos*. Princeton University Press.
- Frederiks, D., et al., 2023. Properties of the Extremely Energetic GRB 221009A from Konus-WIND and SRG/ART-XC Observations. *Astrophys. J. Lett.* 949, L7. doi:10.3847/2041-8213/acd1eb, arXiv:2302.13383.
- Fukushima, T., To, S., Asano, K., Fujita, Y., 2017. Temporal Evolution of the Gamma-ray Burst Afterglow Spectrum for an Observer: GeV–TeV Synchrotron Self-Compton Light Curve. *The Astrophysical Journal* 844, 92. doi:10.3847/1538-4357/aa7b83.
- Gallant, Y.A., Achterberg, A., 1999. Ultra-high-energy cosmic ray acceleration by relativistic blast waves. *Mon. Not. Roy. Astron. Soc.* 305, 6. doi:10.1046/j.1365-8711.1999.02566.x, arXiv:astro-ph/9812316.
- Gill, R., Granot, J., 2022. Gamma-Ray Bursts at TeV Energies: Theoretical Considerations. *Galaxies* 10, 74. doi:10.3390/galaxies10030074.
- Gill, R., Granot, J., 2023. GRB 221009A afterglow from a shallow angular structured jet. *Mon. Not. Roy. Astron. Soc.* 524, L78–L83. doi:10.1093/mnras/slad075, arXiv:2304.14331.
- Gottlieb, O., Bromberg, O., Singh, C.B., Nakar, E., 2020a. The structure of weakly magnetized γ -ray burst jets. *Mon. Not. Roy. Astron. Soc.* 498, 3320–3333. doi:10.1093/mnras/staa2567, arXiv:2007.11590.
- Gottlieb, O., Nakar, E., Bromberg, O., 2020b. The structure of hydrodynamic γ -ray burst jets. *Mon. Not. Roy. Astron. Soc.* 500, 3511–3526. doi:10.1093/mnras/staa3501, arXiv:2006.02466.
- Gould, R.J., 1975. Energy loss of relativistic electrons and positrons traversing cosmic matter. *Astrophys. J.* 196, 689–694. doi:10.1086/153457.
- Groselj, D., Sironi, L., Spitkovsky, A., 2024. Long-term Evolution of Relativistic Unmagnetized Collisionless Shocks. arXiv e-prints, arXiv:2401.02392doi:10.48550/arXiv.2401.02392, arXiv:2401.02392.
- He, H.N., Thodore Zhang, B., Fan, Y.Z., 2024. A detectable ultra-high-energy cosmic ray outburst from GRB 221009A. arXiv e-prints, arXiv:2401.11566doi:10.48550/arXiv.2401.11566, arXiv:2401.11566.
- He, H.N., Zhang, B.B., Wang, X.Y., Li, Z., Mészáros, P., 2012. Origin of the GeV Emission During the X-ray Flaring Activity in GRB 100728A. *Astrophys. J.* 753, 178. doi:10.1088/0004-637X/753/2/178, arXiv:1112.2253.
- Huang, J.K., Huang, X.L., Cheng, J.G., Ren, J., Zhang, L.L., Liang, E.W., 2023a. Hard TeV Gamma-Ray Afterglows of Nearby GRB 190829A as a Tentative Signature of Ultra-high-energy Cosmic Rays Accelerated in Gamma-Ray Burst Jets. *Astrophys. J.* 947, 84. doi:10.3847/1538-4357/acc85f, arXiv:2304.10188.
- Huang, Y., 2022. Time-dependent numerical model for studying the very-high-energy emissions of distant gamma-ray burst GRB 201216C. *Astrophysical Journal* 931, 150. doi:10.3847/1538-4357/ac6d52, arXiv:2204.08208.
- Huang, Y.F., Cheng, K.S., 2003. Gamma-ray bursts: Optical afterglows in the deep Newtonian phase. *Monthly Notices of the Royal Astronomical Society* 341, 263–269. doi:10.1046/j.1365-8711.2003.06430.x.
- Huang, Z.Q., Reville, B., Kirk, J.G., Giacinti, G., 2023b. Prospects for ultra-high-energy particle acceleration at relativistic shocks. *Mon. Not. Roy. Astron. Soc.* 522, 4955–4962. doi:10.1093/mnras/stad1356, arXiv:2304.08132.
- Ioka, K., Nakamura, T., 2018. Can an off-axis gamma-ray burst jet in GW170817 explain all the electromagnetic counterparts? *Progress of Theoretical and Experimental Physics* 2018, 043E02. doi:10.1093/ptep/pty036, arXiv:1710.05905.
- Isravel, H., Begue, D., Pe'er, A., 2023a. Hybrid Emission Modeling of GRB 221009A: Shedding Light on TeV Emission Origins in Long GRBs. *Astrophys. J.* 956, 12. doi:10.3847/1538-4357/acefcd, arXiv:2308.06994.
- Isravel, H., Pe'er, A., Begue, D., 2023b. Proton Synchrotron Origin of the Very-high-energy Emission of GRB 190114C. *Astrophys. J.* 955, 70. doi:10.3847/1538-4357/acec73, arXiv:2210.02363.
- Khangulyan, D., Aharonian, F., Taylor, A.M., 2023. Naked forward shock seen in the TeV afterglow data of GRB221009A. arXiv e-prints, arXiv:2309.00673doi:10.48550/arXiv.2309.00673, arXiv:2309.00673.
- Khangulyan, D., Taylor, A.M., Aharonian, F., 2023. The formation of hard

- very high energy spectra from gamma-ray burst afterglows via two-zone synchrotron self-compton emission. *Astrophysical Journal* 947, 87. doi:10.3847/1538-4357/acc24e, arXiv:2301.08578.
- Kimura, S.S., 2022. Neutrinos from Gamma-ray Bursts. doi:10.48550/arXiv.2202.06480, arXiv:2202.06480.
- Kobayashi, S., 2000. Light Curves of Gamma-Ray Burst Optical Flashes. *Astrophys. J.* 545, 807–812. doi:10.1086/317869, arXiv:astro-ph/0009319.
- Kumar, P., Granot, J., 2003. The Evolution of a Structured Relativistic Jet and Gamma-Ray Burst Afterglow Light Curves. *Astrophys. J.* 591, 1075–1085. doi:10.1086/375186, arXiv:astro-ph/0303174.
- Kumar, P., Zhang, B., 2014. The physics of gamma-ray bursts & relativistic jets. *Phys. Rept.* 561, 1–109. doi:10.1016/j.physrep.2014.09.008, arXiv:1410.0679.
- Laskar, T., et al., 2023. The Radio to GeV Afterglow of GRB 221009A. *Astrophys. J. Lett.* 946, L23. doi:10.3847/2041-8213/acbfad, arXiv:2302.04388.
- Lazzati, D., Perna, R., Morsony, B.J., Lopez-Camara, D., Cantiello, M., Ciolfi, R., Giacomazzo, B., Workman, J.C., 2018. Late time afterglow observations reveal a collimated relativistic jet in the ejecta of the binary neutron star merger gw170817. *Phys. Rev. Lett.* 120, 241103. URL: <https://link.aps.org/doi/10.1103/PhysRevLett.120.241103>, doi:10.1103/PhysRevLett.120.241103.
- Lesage, S., et al., 2023. Fermi-GBM Discovery of GRB 221009A: An Extraordinarily Bright GRB from Onset to Afterglow. *Astrophys. J. Lett.* 952, L42. doi:10.3847/2041-8213/ace5b4, arXiv:2303.14172.
- Li, Z., Dai, Z.G., Lu, T., 2002. Long term neutrino afterglows from gamma-ray bursts. *Astron. Astrophys.* 396, 303–308. doi:10.1051/0004-6361:20021397, arXiv:astro-ph/0208435.
- Liu, R.Y., Zhang, H.M., Wang, X.Y., 2023. Constraints on Gamma-Ray Burst Models from GRB 221009A: GeV Gamma Rays versus High-energy Neutrinos. *Astrophys. J. Lett.* 943, L2. doi:10.3847/2041-8213/acaf5e, arXiv:2211.14200.
- Lucarelli, F., Oganessian, G., Montaruli, T., Branchesi, M., Mei, A., Ronchini, S., Brighenti, F., Banerjee, B., Voutsinas, G.G., 2023. Neutrino search from γ -ray bursts during the prompt and X-ray afterglow phases using 10 years of IceCube public data. *Astron. Astrophys.* 672, A102. doi:10.1051/0004-6361/202244815, arXiv:2208.13792.
- Ma, X.H., et al., 2022. Chapter 1 LHAASO Instruments and Detector technology *. *Chin. Phys. C* 46, 030001. doi:10.1088/1674-1137/ac3fa6.
- Margutti, R., Alexander, K.D., Xie, X., Sironi, L., Metzger, B.D., Kathirgamaraju, A., Fong, W., Blanchard, P.K., Berger, E., MacFadyen, A., Giannios, D., Guidorzi, C., Hajela, A., Chornock, R., Cowperthwaite, P.S., Eftekhari, T., Nicholl, M., Villar, V.A., Williams, P.K.G., Zrake, J., 2018. The Binary Neutron Star Event LIGO/Virgo GW170817 160 Days after Merger: Synchrotron Emission across the Electromagnetic Spectrum. *Astrophys. J. Lett.* 856, L18. doi:10.3847/2041-8213/aab2ad, arXiv:1801.03531.
- Medvedev, M.V., Loeb, A., 1999. Generation of magnetic fields in the relativistic shock of gamma-ray burst sources. *Astrophys. J.* 526, 697–706. doi:10.1086/308038, arXiv:astro-ph/9904363.
- Mészáros, P., 2006. Gamma-Ray Bursts. *Rept. Prog. Phys.* 69, 2259–2322. doi:10.1088/0034-4885/69/8/R01, arXiv:astro-ph/0605208.
- Mészáros, P., Rees, M.J., 1994. Delayed GeV emission from cosmological gamma-ray bursts: Impact of a relativistic wind on external matter. *Monthly Notices of the Royal Astronomical Society* 269, L41–L43. doi:10.1093/mnras/269.1.L41.
- Mészáros, P., Rees, M.J., Wijers, R.A.M.J., 1998. Viewing Angle and Environment Effects in Gamma-Ray Bursts: Sources of Afterglow Diversity. *Astrophys. J.* 499, 301–308. doi:10.1086/305635, arXiv:astro-ph/9709273.
- Miceli, D., Nava, L., 2022. Gamma-ray bursts afterglow physics and the VHE domain. *Galaxies* 10, 66. doi:10.3390/galaxies10030066, arXiv:2205.12146.
- Mirabal, N., 2022. Secondary GeV-TeV emission from ultra-high-energy cosmic rays accelerated by GRB 221009A. *Mon. Not. Roy. Astron. Soc.* 519, L85–L86. doi:10.1093/mnras/1/slac157, arXiv:2210.14243.
- Miralda-Escudé, J., Waxman, E., 1996. Signatures of the Origin of High-Energy Cosmic Rays in Cosmological Gamma-Ray Bursts. *The Astrophysical Journal* 462. doi:10.1086/310042.
- Murase, K., 2007. High energy neutrino early afterglows from gamma-ray bursts revisited. *Physical Review D* 76, 123001. doi:10.1103/PhysRevD.76.123001.
- Murase, K., Dermer, C.D., Takami, H., Migliori, G., 2012. Blazars as Ultra-high-energy Cosmic-ray Sources: Implications for TeV Gamma-Ray Observations. *Astrophys. J.* 749, 63. doi:10.1088/0004-637X/749/1/63, arXiv:1107.5576.
- Murase, K., Ioka, K., Nagataki, S., Nakamura, T., 2008. High-energy cosmic-ray nuclei from high- and low-luminosity gamma-ray bursts and implications for multimessenger astronomy. *Physical Review D* 78, 023005. doi:10.1103/PhysRevD.78.023005.
- Murase, K., Mukhopadhyay, M., Kheirandish, A., Kimura, S.S., Fang, K., 2022. Neutrinos from the Brightest Gamma-Ray Burst? *Astrophys. J. Lett.* 941, L10. doi:10.3847/2041-8213/aca3ae, arXiv:2210.15625.
- Murase, K., Takami, H., 2009. IMPLICATIONS OF ULTRA-HIGH-ENERGY COSMIC RAYS FOR TRANSIENT SOURCES IN THE AUGER ERA. *The Astrophysical Journal* 690, L14–L17. doi:10.1088/0004-637X/690/1/L14.
- Murase, K., Toma, K., Yamazaki, R., Mészáros, P., 2011. ON THE IMPLICATIONS OF LATE INTERNAL DISSIPATION FOR SHALLOW-DECAY AFTERGLOW EMISSION AND ASSOCIATED HIGH-ENERGY GAMMA-RAY SIGNALS. *The Astrophysical Journal* 732, 77. URL: <https://iopscience.iop.org/article/10.1088/0004-637X/732/2/77>, doi:10.1088/0004-637X/732/2/77.
- Murase, K., Toma, K., Yamazaki, R., Nagataki, S., Ioka, K., 2010. High-energy emission as a test of the prior emission model for gamma-ray burst afterglows. *Monthly Notices of the Royal Astronomical Society* 402, L54–L58. doi:10.1111/j.1745-3933.2009.00799.x, arXiv:0910.0232.
- Murase, K., Toomey, M.W., Fang, K., Oikonomou, F., Kimura, S.S., Hotokezaka, K., Kashiyama, K., Ioka, K., Mészáros, P., 2018. Double neutron star mergers and short gamma-ray bursts: Long-lasting high-energy signatures and remnant dichotomy. *Astrophysical Journal* 854, 60. doi:10.3847/1538-4357/aaa48a, arXiv:1710.10757.
- Nava, L., Sironi, L., Ghisellini, G., Celotti, A., Ghirlanda, G., 2013. Afterglow emission in gamma-ray bursts – I. Pair-enriched ambient medium and radiative blast waves. *Monthly Notices of the Royal Astronomical Society* 433, 2107–2121. doi:10.1093/mnras/stt872.
- Noda, K., Parsons, R.D., 2022. Gamma-Ray Bursts at TeV Energies: Observational Status. *Galaxies* 10, 7. doi:10.3390/galaxies10010007.
- O'Connor, B., et al., 2023. A structured jet explains the extreme GRB 221009A. *Sci. Adv.* 9, ad1405. doi:10.1126/sciadv.ad1405, arXiv:2302.07906.
- Razzaque, S., 2013. Long-lived PeV–EeV neutrinos from gamma-ray burst blastwave. *Phys. Rev. D* 88, 103003. doi:10.1103/PhysRevD.88.103003, arXiv:1307.7596.
- Ren, J., Wang, Y., Dai, Z.G., 2023. Jet Structure and Burst Environment of GRB 221009A. *arXiv e-prints*, arXiv:2310.15886doi:10.48550/arXiv.2310.15886, arXiv:2310.15886.
- Ren, J., Wang, Y., Zhang, L.L., Dai, Z.G., 2023. The Possibility of Modeling the Very High Energy Afterglow of GRB 221009A in a Wind Environment. *The Astrophysical Journal* 947, 53. doi:10.3847/1538-4357/acc57d.
- Rossi, E., Lazzati, D., Rees, M.J., 2002. Afterglow lightcurves, viewing angle and the jet structure of gamma-ray bursts. *Mon. Not. Roy. Astron. Soc.* 332, 945. doi:10.1046/j.1365-8711.2002.05363.x, arXiv:astro-ph/0112083.
- Rudolph, A., Petropoulou, M., Winter, W., Bošnjak, v., 2023. Multi-messenger Model for the Prompt Emission from GRB 221009A. *Astrophys. J. Lett.* 944, L34. doi:10.3847/2041-8213/acb6d7, arXiv:2212.00766.
- Ryan, G., van Eerten, H., Piro, L., Troja, E., 2020. Gamma-Ray Burst Afterglows in the Multimessenger Era: Numerical Models and Closure Relations. *The Astrophysical Journal* 896, 166. doi:10.3847/1538-4357/ab93cf.
- Ryan, G., van Eerten, H., Troja, E., Piro, L., O'Connor, B., Ricci, R., 2023. Modelling of Long-Term Afterglow Counterparts to Gravitational Wave Events: The Full View of GRB 170817A. *arXiv e-prints*, arXiv:2310.02328doi:10.48550/arXiv.2310.02328, arXiv:2310.02328.
- Salafia, O.S., et al., 2022. Multiwavelength view of the close-by GRB 190829A sheds light on gamma-ray burst physics. *Astrophysical Journal, Letters to the Editor* 931, L19. doi:10.3847/2041-8213/ac6c28, arXiv:2106.07169.
- Saldana-Lopez, A., Domínguez, A., Pérez-González, P.G., Finke, J., Ajello, M., Primack, J.R., Paliya, V.S., Desai, A., 2021. An observational determination of the evolving extragalactic background light from the multiwave-

- length *HST*/CANDELS survey in the *Fermi* and CTA era. *Monthly Notices of the Royal Astronomical Society* 507, 5144–5160. doi:10.1093/mnras/stab2393.
- Sari, R., 1997. Hydrodynamics of Gamma-Ray Burst Afterglow. *The Astrophysical Journal* 489, L37–L40. URL: <https://iopscience.iop.org/article/10.1086/310957>, doi:10.1086/310957.
- Sari, R., Esin, A.A., 2001. On the Synchrotron self-compton emission from relativistic shocks and its implications for gamma-ray burst afterglows. *Astrophys. J.* 548, 787–799. doi:10.1086/319003.
- Sari, R., Piran, T., 1995. Hydrodynamic Timescales and Temporal Structure of Gamma-Ray Bursts. *The Astrophysical Journal* 455. URL: <https://iopscience.iop.org/article/10.1086/309835>, doi:10.1086/309835.
- Sato, Y., Murase, K., Ohira, Y., Yamazaki, R., 2023a. Two-component jet model for multiwavelength afterglow emission of the extremely energetic burst GRB 221009A. *Mon. Not. Roy. Astron. Soc.* 522, L56–L60. doi:10.1093/mnras/1slad038, arXiv:2212.09266.
- Sato, Y., Obayashi, K., Zhang, B.T., Tanaka, S.J., Murase, K., Ohira, Y., Yamazaki, R., 2023b. Synchrotron self-compton emission in the two-component jet model for gamma-ray bursts. *JHEAp* 37, 51–61. doi:10.1016/j.jheap.2022.12.004, arXiv:2208.13987.
- Shen, J.Y., Zou, Y.C., Chen, A.M., Gao, D.Y., 2023. What absorbs the early TeV photons of GRB 221009A? *Monthly Notices of the Royal Astronomical Society* doi:10.1093/mnras/1slad188, arXiv:2308.10477.
- Sironi, L., Giannios, D., 2013. A LATE-TIME FLATTENING OF LIGHT CURVES IN GAMMA-RAY BURST AFTERGLOWS. *The Astrophysical Journal* 778, 107. doi:10.1088/0004-637X/778/2/107.
- Sironi, L., Keshet, U., Lemoine, M., 2015. Relativistic Shocks: Particle Acceleration and Magnetization. *Space Science Reviews* 191, 519–544. doi:10.1007/s11214-015-0181-8.
- Sironi, L., Spitkovsky, A., Arons, J., 2013. The Maximum Energy of Accelerated Particles in Relativistic Collisionless Shocks. *Astrophys. J.* 771, 54. doi:10.1088/0004-637X/771/1/54, arXiv:1301.5333.
- Svensson, R., 1987. Non-thermal pair production in compact X-ray sources : first-order Compton cascades in soft radiation fields. *Monthly Notices of the Royal Astronomical Society* 227, 403–451. doi:10.1093/mnras/227.2.403.
- Takahashi, K., Ioka, K., 2020. Inverse reconstruction of jet structure from off-axis gamma-ray burst afterglows. *Monthly Notices of the Royal Astronomical Society* 497, 1217–1235. doi:10.1093/mnras/staa1984.
- Takahashi, K., Ioka, K., Ohira, Y., van Eerten, H.J., 2022. Probing particle acceleration at trans-relativistic shocks with off-axis gamma-ray burst afterglows. *Monthly Notices of the Royal Astronomical Society* 517, 5541–5559. doi:10.1093/mnras/stac3022, arXiv:2208.06274.
- Takami, H., Murase, K., 2012. The Role of Structured Magnetic Fields on Constraining Properties of Transient Sources of Ultra-high-energy Cosmic Rays. *Astrophys. J.* 748, 9. doi:10.1088/0004-637X/748/1/9, arXiv:1110.3245.
- Toma, K., Wu, X.F., Mészáros, P., 2009. An up-scattered cocoon emission model of Gamma-Ray Burst high-energy lags. *Astrophys. J.* 707, 1404–1416. doi:10.1088/0004-637X/707/2/1404, arXiv:0905.1697.
- Totani, T., 1998a. TeV burst of gamma-ray bursts and ultrahigh-energy cosmic rays. *Astrophys. J. Lett.* 509, L81–L84. doi:10.1086/311772, arXiv:astro-ph/9810206.
- Totani, T., 1998b. Very strong TeV emission as gamma-ray burst afterglows. *Astrophys. J. Lett.* 502, L13. doi:10.1086/311489, arXiv:astro-ph/9805264.
- Troja, E., Piro, L., Ryan, G., van Eerten, H., Ricci, R., Wieringa, M.H., Lotti, S., Sakamoto, T., Cenko, S.B., 2018. The outflow structure of GW170817 from late-time broad-band observations. *Monthly Notices of the Royal Astronomical Society* 478, L18–L23. doi:10.1093/mnras/1sly061, arXiv:1801.06516.
- van Eerten, H., Zhang, W., MacFadyen, A., 2010. OFF-AXIS GAMMA-RAY BURST AFTERGLOW MODELING BASED ON A TWO-DIMENSIONAL AXISYMMETRIC HYDRODYNAMICS SIMULATION. *The Astrophysical Journal* 722, 235–247. doi:10.1088/0004-637X/722/1/235.
- Venters, T.M., Reno, M.H., Krizmanic, J.F., Anchordoqui, L.A., Guépin, C., Olinto, A.V., 2020. POEMMA’s Target of Opportunity Sensitivity to Cosmic Neutrino Transient Sources. *Phys. Rev. D* 102, 123013. doi:10.1103/PhysRevD.102.123013, arXiv:1906.07209.
- Veres, P., Mészáros, P., 2014. Prospects for GeV-TeV detection of short gamma-ray bursts with extended emission. *Astrophys. J.* 787, 168. doi:10.1088/0004-637X/787/2/168, arXiv:1312.0590.
- Vietri, M., 1996. Coronal gamma-ray bursts as the sources of ultra-high-energy cosmic rays? *Monthly Notices of the Royal Astronomical Society* 278, L1–L4. doi:10.1093/mnras/278.1.L1.
- Wang, X.Y., Li, Z., Mészáros, P., 2006. GeV-TeV and x-ray flares from gamma-ray burst. *Astrophys. J. Lett.* 641, L89–L92. doi:10.1086/504151, arXiv:astro-ph/0601229.
- Wang, X.Y., Liu, R.Y., Zhang, H.M., Xi, S.Q., Zhang, B., 2019. Synchrotron Self-Compton Emission from External Shocks as the Origin of the Sub-TeV Emission in GRB 180720B and GRB 190114C. *Astrophys. J.* 884, 117. doi:10.3847/1538-4357/ab426c, arXiv:1905.11312.
- Waxman, E., 1995. Cosmological Gamma-Ray Bursts and the Highest Energy Cosmic Rays. *Physical Review Letters* 75, 386–389. doi:10.1103/PhysRevLett.75.386.
- Waxman, E., Bahcall, J.N., 2000. Neutrino Afterglow from Gamma-Ray Bursts: $\sim 10^{18}$ eV. *The Astrophysical Journal* 541, 707–711. doi:10.1086/309462.
- Wei, Y., Zhang, B.T., Murase, K., 2023. Multiwavelength afterglow emission from bursts associated with magnetar flares and fast radio bursts. *Mon. Not. Roy. Astron. Soc.* 524, 6004–6014. doi:10.1093/mnras/stad2122, arXiv:2301.10184.
- Yi, S.X., Wu, X.F., Zou, Y.C., Dai, Z.G., 2020. The Bright Reverse Shock Emission in the Optical Afterglows of Gamma-ray Bursts in a Stratified Medium. *Astrophys. J.* 895, 94. doi:10.3847/1538-4357/ab8a53, arXiv:2004.08577.
- Zeolla, A., et al., 2023. Sensitivity of BEACON to Point Sources of Ultrahigh Energy Neutrinos. *PoS ICRC2023*, 1020. doi:10.22323/1.444.1020.
- Zhang, B., 2018. *The Physics of Gamma-Ray Bursts*. First ed., Cambridge University Press. doi:10.1017/9781139226530.
- Zhang, B., 2019. Extreme emission seen from γ -ray bursts. *Nature* 575, 448–449. doi:10.1038/d41586-019-03503-6.
- Zhang, B., Dai, X., Lloyd-Ronning, N.M., Mészáros, P., 2004. Quasi-universal Gaussian Jets: A Unified Picture for Gamma-Ray Bursts and X-Ray Flashes. *Astrophys. J. Lett.* 601, L119–L122. doi:10.1086/382132, arXiv:astro-ph/0311190.
- Zhang, B., Kobayashi, S., 2005. Gamma-ray burst early afterglows: Reverse shock emission from an arbitrarily magnetized ejecta. *Astrophys. J.* 628, 315–334. doi:10.1086/429787, arXiv:astro-ph/0404140.
- Zhang, B., Kobayashi, S., Meszaros, P., 2003. Gamma-ray burst early optical afterglow: Implications for the initial Lorentz factor and the central engine. *Astrophys. J.* 595, 950–954. doi:10.1086/377363, arXiv:astro-ph/0302525.
- Zhang, B., Meszaros, P., 2001. High-Energy Spectral Components in Gamma-Ray Burst Afterglows. *The Astrophysical Journal* 559, 110–122. doi:10.1086/322400.
- Zhang, B., Meszaros, P., 2002. Gamma-ray burst beaming: a universal configuration with a standard energy reservoir? *Astrophys. J.* 571, 876–879. doi:10.1086/339981, arXiv:astro-ph/0112118.
- Zhang, B., Wang, X.Y., Zheng, J.H., 2023. The BOAT GRB 221009A: a Poynting-Flux-Dominated Narrow Jet Surrounded by a Matter-Dominated Structured Jet Wing. *arXiv e-prints*, arXiv:2311.14180doi:10.48550/arXiv.2311.14180, arXiv:2311.14180.
- Zhang, B.T., Murase, K., Ioka, K., Song, D., Yuan, C., Mészáros, P., 2023. External Inverse-compton and Proton Synchrotron Emission from the Reverse Shock as the Origin of VHE Gamma Rays from the Hyper-bright GRB 221009A. *The Astrophysical Journal Letters* 947, L14. doi:10.3847/2041-8213/acc79f.
- Zhang, B.T., Murase, K., Kimura, S.S., Horiuchi, S., Mészáros, P., 2018. Low-luminosity gamma-ray bursts as the sources of ultrahigh-energy cosmic ray nuclei. *Physical Review D* 97, 083010. doi:10.1103/PhysRevD.97.083010.
- Zhang, B.T., Murase, K., Veres, P., Mészáros, P., 2021a. External Inverse-Compton Emission from Low-luminosity Gamma-Ray Bursts: Application to GRB 190829A. *The Astrophysical Journal* 920, 55. doi:10.3847/1538-4357/ac0cfc.
- Zhang, B.T., Murase, K., Yuan, C., Kimura, S.S., Mészáros, P., 2021b. External Inverse-Compton Emission Associated with Extended and Plateau Emission of Short Gamma-Ray Bursts: Application to GRB 160821B. *The Astrophysical Journal Letters* 908, L36. doi:10.3847/2041-8213/abe0b0.

- Zhang, L.L., Ren, J., Huang, X.L., Liang, Y.F., Lin, D.B., Liang, E.W., 2021. Nearby SN-associated GRB 190829A: Environment, Jet Structure, and VHE Gamma-Ray Afterglows. *Astrophys. J.* 917, 95. doi:10.3847/1538-4357/ac0c7f, arXiv:2106.03466.
- Zhang, W., MacFadyen, A., 2009. The Dynamics and Afterglow Radiation of Gamma-Ray Bursts. I. Constant Density Medium. *Astrophys. J.* 698, 1261–1272. doi:10.1088/0004-637X/698/2/1261, arXiv:0902.2396.
- Zheng, J.H., Wang, X.Y., Liu, R.Y., Zhang, B., 2023. A Two-component Jet Model for the TeV and Multi-wavelength Afterglows of GRB 221009A. arXiv e-prints, arXiv:2310.12856doi:10.48550/arXiv.2310.12856, arXiv:2310.12856.